JGP Journal of General Physiology

ARTICLE

A novel, patient-derived RyR1 mutation impairs muscle function and calcium homeostasis in mice

Sofia Benucci[1], Alexis Ruiz[1], Martina Franchini[1], Lucia Ruggiero[2], Dario Zoppi[2], Rebecca Sitsapesan[3], Chris Lindsay[3], Pawel Pelczar[4], Laura Pietrangelo[5], Feliciano Protasi[5], Susan Treves[1,6], and Francesco Zorzato[1,6]

RYR1 **is the most commonly mutated gene associated with congenital myopathies, a group of early-onset neuromuscular conditions of variable severity. The functional effects of a number of dominant *RYR1* mutations have been established; however, for recessive mutations, these effects may depend on multiple factors, such as the formation of a hypomorphic allele, or on whether they are homozygous or compound heterozygous. Here, we functionally characterize a new transgenic mouse model knocked-in for mutations identified in a severely affected child born preterm and presenting limited limb movement. The child carried the homozygous c.14928C>G *RYR1* mutation, resulting in the p.F4976L substitution. In vivo and ex vivo assays revealed that homozygous mice fatigued sooner and their muscles generated significantly less force compared with their WT or heterozygous littermates. Electron microscopy, biochemical, and physiological analyses showed that muscles from RyR1 p.F4976L homozygous mice have the following properties: (1) contain fewer calcium release units and show areas of myofibrillar degeneration, (2) contain less RyR1 protein, (3) fibers show smaller electrically evoked calcium transients, and (4) their SR has smaller calcium stores. In addition, single-channel recordings indicate that RyR1 p.F4976L exhibits higher Po in the presence of 100 µM [Ca^{2+}]. Our mouse model partly recapitulates the clinical picture of the homozygous human patient and provides significant insight into the functional impact of this mutation. These results will help understand the pathology of patients with similar *RYR1* mutations.**

Introduction

Congenital myopathies (CMs) are a group of early-onset, neuromuscular diseases of variable severity, normally present at birth with a prevalence of 0.6–2 per 100,000 live births (Nicolau et al., 2019), characterized by a stable or pejorative progressive phenotype and typical muscle biopsy findings (Tubridy et al., 2001). Patients with CMs usually present specific symptoms, including weakness of axial and/or proximal muscles; in some cases, cardiorespiratory and extraocular muscles (EOMs) are also affected (Tubridy et al., 2001; Dowling et al., 2018; Jungbluth et al., 2018). Mutations in ∼20 genes have been listed as the primary cause of CMs. Not unexpectedly, however, mutations in genes encoding for proteins involved in excitation–contraction coupling (ECC), calcium homeostasis, and myofilaments are mainly responsible for CMs (Treves et al., 2008; Jungbluth et al., 2018). Among these, mutations in *RYR1*, the gene encoding the ryanodine receptor type 1 (RyR1) calcium channel, are the most common form of non-dystrophic muscle disorders in humans (Lawal et al., 2020). Indeed, *RYR1*-related myopathies (RYR1-RMs) have a calculated US prevalence of 1:90,000 (Lawal et al., 2018).

The skeletal muscle RyR1 Ca^{2+} channel plays an essential role in the process of ECC whereby an electrical signal occurring at the plasma membrane is converted into a chemical signal, resulting in muscle contraction (Ríos and Pizarro, 1991; Calderón et al., 2014; Shishmarev, 2020). In skeletal muscle, the membrane action potential is sensed by dihydropyridine receptors (DHPR) an L-type Ca^{2+} channels located on transverse tubules (Endo, 1985; Melzer et al., 1995). Upon sensing the incoming action potential, these undergo a conformational change, thereby activating RyR1s located on the terminal cisternae of the sarcoplasmic reticulum (SR) (Fleischer and Inui, 1989; Franzini-Armstrong and Jorgensen, 1994; Calderón et al., 2014; Shishmarev, 2020), resulting in release of Ca^{2+} from the SR into the myoplasm (Ríos and Pizarro, 1991; Calderón et al., 2014; Shishmarev, 2020). This Ca^{2+} binds to the contractile machinery, thereby initiating muscle contraction, and is subsequently

[1]Departments of Biomedicine and Neurology, Basel University Hospital, Basel, Switzerland; [2]Dipartimento di Neuroscienze, Scienze Riproduttive ed Odontostomatologiche, Università degli Studi di Napoli Federico II, Napoli, Italy; [3]Department of Pharmacology, University of Oxford, Oxford, UK; [4]Center for Transgenic Models, University of Basel, Basel, Switzerland; [5]DMSI, Department of Medicine and Aging Sciences and CAST, Center for Advanced Studies and Technology, University G. d'Annunzio of Chieti-Pescara, Chieti, Italy; [6]Department of Life Science and Biotechnology, University of Ferrara, Ferrara, Italy.

Rebecca Sitsapesan died on June 2, 2022. Correspondence to Francesco Zorzato: fzorzato@usb.ch, zor@unife.it.

pumped back into the SR by the sarco/endoplasmic reticulum Ca^{2+}-ATPase (SERCA) pumps (Fleischer and Inui, 1989; Calderón et al., 2014; Agrawal et al., 2018), allowing the muscles to undergo another round of contraction–relaxation cycle.

RYR1-RMs can be classified depending on their histological features, the position of the mutation, and their inheritance pattern. Indeed, mutations can affect the RyR1 differently, changing the biophysical properties, stability, and expression levels (Treves et al., 2008). Gain-of-function mutations, such as those associated with human malignant hyperthermia susceptibility (MH—MIM #145600), are mostly dominant and cause hyperactivity of the Ca^{2+} channel in the presence of external triggers (for example, volatile anesthetics, hot environment, exercise), with consequent hypermetabolism, muscle rigidity, and increased body temperature (McCarthy et al., 2000). Loss-of-function mutations such as those associated with the central core disease (CCD—MIM #117000) are mostly dominant, causing a weak muscle phenotype either because of Ca^{2+} leakage or ECC-uncoupling (Lynch et al., 1999; Dirksen and Avila, 2004; Treves et al., 2008). Recessive mutations cause the most severe forms of RYR1-RM and are often accompanied by a decrease in RyR1 protein content in the muscle fibers. They have been reported in patients with centronuclear myopathy (CNM) and multiminicore disease (MmD—MIM #255320) and are present as homozygous or compound heterozygous mutations (Zorzato et al., 2007; Jungbluth et al., 2008; Elbaz et al., 2019b). Patients with recessive *RYR1* mutations often present reduced fetal movements, are hypotonic at birth, and show feeding and respiratory difficulties, often requiring gastrostomy and non-invasive ventilation. A large proportion of patients with recessive *RYR1* mutations characteristically also exhibit facial weakness, ptosis, and/or extraocular muscle involvement; interestingly, of all patients with any form of recessive *RYR1* mutations ≈40% either have ptosis or ophthalmoplegia, whereas this number increases to ≈70% in the case of compound heterozygous patients carrying at least one hypomorphic allele (Amburgey et al., 2013; Sarkozy et al., 2023).

To extend the knowledge on the pathological mechanisms brought by recessive RYR1-RMs, we recently created the *Ryr1* p.F4976L homozygous mouse model (referable as Ho), which is knocked-in for a *Ryr1* mutation isogenic to that identified in a severely affected child. The proband was a severely affected male, born prematurely to nonconsanguineous Caucasian parents. The patient presented with generalized floppiness at birth, muscle weakness, and the absence of sucking reflex/poor feeding capacity and required a gastrostomy. Initially diagnosed as dystrophic, the child was later found to harbor the homozygous RyR1 p.F4976L mutation in exon 104 (c.14928C>G), having inherited the single mutated alleles from each of his healthy, non-affected parents. Today, the child shows progressive phenotypic improvement, is able to perform basic movements, and feeds autonomously. The aim of this article is to understand the mechanisms leading to the severe muscle impairment caused by the homozygous RyR1 p.F4976L mutation by studying the physiological and biochemical characteristics of the transgenic *Ryr1* p.F4976L mouse model.

Materials and methods

Compliance with ethical standards and experimental performance

All experiments were approved by the Cantonal Veterinary Authority of Basel Stadt (BS Kantonales Veterinäramt permit numbers 1728, 2115, and 2950). Experimental procedures were conducted on 6–22-wk-old male Ho, Het, and WT littermate mice, unless otherwise stated.

Generation of transgenic RyR1 p.F4976L mice and genotyping

The RyR1 p.F4976L transgenic mouse line was generated by the Center for Transgenic Models of Basel by the CRISPR/Cas9 technique as previously described (Elbaz et al., 2019a). The c.14928C>G point mutation was inserted in the *Ryr1* gene using the oligo sequence guide: 5′-GTCACCGAGCCTTCCTTGACTCTG ACATCTTCCGTTGTCCTCAGACCAAGTGCTTCATCTGTGGAA TAGGCAGTGACTACTTCGACACAACACCACATGGGCTCGAGA CCCACACTCTAGAAGAGCACAACCTAGCCAATTACATGTGAG TGTGGGAAGTGATGGGTGATCAGAGGGTGGGAGTGAGCCTGT TGATAGCC-3′. The presence of the mutation was confirmed in the founder mice by direct genomic DNA sequencing. Mutant mice were mated with WT C57BL/6 mice to produce the F1 and subsequent generations, and the presence of the mutation was confirmed at the genomic and cDNA levels using the primers listed in Table S1. For all subsequent generations, the genotype of the mice was determined by PCR on genomic DNA with GoTaq DNA polymerase (Promega) using the primers listed in Table S1 and the following PCR conditions: initial denaturation 5′ at 95°C, followed by 35 cycles of denaturation 15″ at 95°C, annealing 30″ at 62°C, extension 1′ at 72°C, followed by a final elongation step of 5′ at 72°C. The amplified DNA product was then digested with the restriction enzyme *XhoI* (New England Biolabs), and the presence of the mutation was confirmed by running the samples on a 7.5% polyacrylamide gel (Fig. S1).

Real-time qPCR

RNA was extracted from freshly isolated extensor digitorum longus (EDL, fast twitch), soleus (slow twitch), and extraocular (EOMs, specialized) muscles as previously described (Elbaz et al., 2019a; Elbaz et al., 2019b). Briefly, muscles were homogenized in TRIzol (15596026; Thermo Fisher Scientific), treated with DNase I (18068-015; Invitrogen), and then 1 µg of RNA was retro-transcribed into cDNA using the high-capacity cDNA reverse transcription kit (4368814; Applied Biosystems), following the manufacturer's recommendations. Transcript levels were quantified using the Power SYBR Green reagent master mix (4367659; Applied Biosystems) on an Applied Biosystems 7500 apparatus. Transcript analysis was based on the comparative method of the ΔΔCt, and each reaction was performed in duplicate and averaged and the relative abundance of each transcript was normalized to the expression of the housekeeper gene actinin (*Actn2*). Primers are listed in Table S1.

In vivo muscle performance

In vivo muscle performance was assessed using the voluntary running wheel, forelimb grip strength, and treadmill exhaustion test. For the voluntary running wheel, 10–13-wk-old male mice

were placed singly for 22 days in cages equipped with running wheels as previously described (Elbaz et al., 2020). The revolution of the wheels was recorded by reed sensors connected to an I-7053D digital-input module (Spectra) connected to a regular computer to be recorded and processed by the "mouse running" software developed at Santhera Pharmaceuticals. The resulting data were used to calculate the cumulative distance (in km) and average speed (km/h) of each mouse. The forelimb grip strength was measured once per week over a period of 12 wk in male mice starting from the age of 6 wk using the Grip Strength Meter from Columbus Instruments, as previously described (Ruiz et al., 2022). Mean grip force was calculated as the mean of five measurements performed on the same day. The treadmill exhaustion test was performed on 12–13-wk-old male mice using the Treadmill Exer 3/6 (Columbus Instruments), adapting the exhaustion test protocol from Pérez-Schindler et al. (2017) and Castro and Kuang (2017). Briefly, mice were adapted to the treadmill for two consecutive days. On the first day, mice were placed on the treadmill by running at 0, 5, 7.5, and 10 m/min for 5 min each at 5° inclination. On the second day, mice were adapted by running at 0, 5, 7.5, 10, and 12.5 m/min for 5 min each at 5° inclination. On the third day, the maximum running capacity was tested by a sequential increase in running speed with the following protocol: 5 min at 0 m/min, 5 min at 5 m/min, 3 min at 8 m/min followed by 2 m/min increase every 3 min until 28 m/min, from where speed is increased 2 m/min every 10 min until exhaustion, all at 5° inclination.

Ex vivo isometric force measurement in EDL and soleus muscles

The mechanical properties of EDL and soleus muscles from WT and transgenic mice were determined as previously described using a force transducer (Heidelberg Scientific Instruments) (Mosca et al., 2013). Muscles were stimulated for 1.0 ms with 15 V for twitch stimulation. For tetanic stimulation, EDL muscles were stimulated for 400 ms at 50, 100, and 150 Hz, while soleus muscles were stimulated for 1,100 ms at 50, 100, and 120 Hz. The resulting force was digitalized at 4 kHz by using an AD Instrument converter. The specific force was normalized for the cross-section area (CSA) of the muscle using the following formula: CSA = (wet muscle weight mg)/(muscle length mm*1.06 mg/mm^3).

FDB muscle single fibers isolation and intracellular calcium measurements

Intracellular [Ca^{2+}] measurements were performed on single flexor digitorum brevis (FDB) muscle fibers isolated as previously described (Elbaz et al., 2019a). The resting [Ca^{2+}] was measured in fibers loaded with 5 µM fura-2 AM (Invitrogen; Thermo Fisher Scientific) using an inverted Axiovert fluorescent microscope, as previously described (Rokach et al., 2015; Elbaz et al., 2019a). FDB fibers were pretreated for 10 min either with DMSO (4 µl in 2 ml Tyrode's solution) or with 10 µM BTP2 dissolved in DMSO to block calcium influx (Wei-LaPierre et al., 2022).

For electrically induced Ca^{2+} transients, fibers were loaded with 10 µM low-affinity calcium indicator Mag-Fluo-4 AM (Thermo Fisher Scientific) plus 50 µM N-benzyl-p-toluene sulfonamide (BTS; Tocris), as previously described (Elbaz et al., 2019a). Measurements were carried out with a Nikon Eclipse inverted fluorescent microscope equipped with a 20× PH1 DL magnification objective. The light signals originating from a spot of 1 mm diameter of the visual field of FDB fibers were converted into electrical signals by a photomultiplier (Myotronic Heidelberg). Fibers were excited at 480 nm and then stimulated either with a single pulse of 50 V with a duration of 1 ms or with a train of pulses of 50 V with a duration of 300 ms delivered at 100 Hz. Fluorescent signals were acquired using PowerLab Chart7. Changes in fluorescence were calculated as ΔF/F0 = (Fmax – Frest)/(Frest), kinetic parameters including time to peak (TTP) and half-time to peak (HTTP) were analyzed as previously described (Eckhardt et al., 2019), and τ1 and τ2 were calculated as described by Calderon et al. (2009) using the Clampfit v.10.7 software (Molecular Devices Inc). FDB fibers were isolated from four to six mice per group and results were averaged (Mosca et al., 2013). Total SR Ca^{2+} stores were determined as described (Tjondrokoesoemo et al., 2011; Michelucci et al., 2020). Briefly, the fibers were loaded in Tyrode solution with 5 µM Mag-Fluo-4 AM (Thermo Fisher Scientific) for 10 min at 19°C. The fibers were then rinsed and treated with a cocktail of: 40 µM BTS, 2 mM EGTA, 10 µM ionomycin, 30 µM CPA (cyclopiazonic acid, Calbiochem), and 100 µM La^{3+}. Changes in fluorescence were followed using a 20× objective Zeiss Axiovert fluorescent microscope, with an emission filter of 500–530 nm.

Western blotting and biochemical analysis

Total homogenates of EDL, soleus, and EOM muscles of WT and Ho mice were prepared as described (Saito et al., 1984); protein concentration was determined using the Bradford method (500-0006; BioRad) using BSA as the standard. Proteins were separated on 5% (RyR1, Cav1.1,), 7.5% (SERCA1 and SERCA2), 10% (JP-45, Casq1, Casq2, Stac3), and Tris-Tricine (parvalbumin) SDS-PAG, transferred onto nitrocellulose, and Western blotting was performed as previously described (Rokach et al., 2015; Elbaz et al., 2019a). Membranes were incubated with primary antibodies (Table S2), followed by incubation with peroxidase conjugates (Table S2), and the immunopositive bands were visualized by chemiluminescence using the WesternBright ECL HRP Substrate (Witec AG). Images of the blots were taken with the Fusion Solo S (Witec AG) and densitometry was performed using the GelAnalyser software (GelAnalyzer 2010a [http://www.gelanalyzer.com] by Istvan Lazar Jr., PhD, and Istvan Lazar Sr., PhD, CSc). Band intensities were normalized for myosin heavy chain (MyHC) (all isoforms) content. MyHC isoforms were identified on Coomassie Brilliant Blue stained-high-resolution acrylamide gels as previously described (Talmadge and Roy, 1993; Kohn and Myburgh, 2006).

Histological procedures

EDL and soleus muscles were isolated, embedded in OCT (Sigma-Aldrich), deep-frozen in 2-methylbutane (Sigma-Aldrich), and stored at −80°C. Transversal 10-µm sections were obtained using a Leica Cryostat (CM1950), starting from the belly of the muscles. Sections were stained as described by Delezie et al. (2019) (for antibodies see Table S2) and images were taken

with an Eclipse Ti2 Nikon Fluorescence microscope equipped with a 10× air objective. For each genotype (WT and Ho), three to four muscles were imaged. Images were segmented (Stringer et al., 2021; Waisman et al., 2021) and analyzed with Fiji (Rueden et al., 2017) plugins developed by Delezie et al. (2019) to obtain fiber distribution and fiber minimal ferret, meaning the closest possible distance between the two parallel tangents of an object.

Single-channel recordings and analysis

Hindlimb muscles from WT and Ho 11–12-wk-old male and female mice were dissected and prepared as previously described (El-Ajouz et al., 2017). RyR1 channels were embedded into planar phosphatidylethanolamine lipid bilayers as previously described (Sitsapesan et al., 1991), and the channel current fluctuations of the channel in response to increasing [Ca^{2+}] were recorded under voltage clamp conditions as previously described (Lee et al., 2015; Elbaz et al., 2019a). In brief, the *cis*(cytosolic) chamber was made with 250 mM HEPES, 80 mM TRIS, and 3 µM free Ca^{2+}, pH 7.2; the *trans*(luminal) chamber was made with 250 mM glutamic acid, 10 mM HEPES, pH 7.2, and Ca (OH_2) (free [Ca^{2+}] ∼50 mM at 21°C). The free [Ca^{2+}] and pH were measured using a Ross-type electrode (Orion 81-55; Thermo Fisher Scientific) and were maintained constant as previously described (Sitsapesan et al., 1991). Single-channel recordings were digitalized and the open probability (Po) was determined as described (Colquhoun and Sigworth, 1995; Venturi et al., 2014). The Po reported in the figures refers to the value determined over a 3-min period for that channel. In the case of multiple channels incorporated into the lipid bilayer, the average Po (total Po divided by the number of channels) was reported.

Preparation of samples for electron microscopy (EM) analysis

EDL and soleus muscles were dissected from WT (n = 3) and Ho (n = 3) 11–12-wk-old male mice, fixed at room temperature with 3.5% glutaraldehyde in 0.1 M NaCaCO buffer (pH 7.2), and stored in this fixative at 4°C (Pietrangelo et al., 2015, 2019). Fixed muscles were post-fixed in 2% OsO_4 for 1–2 h, rinsed with 0.1 M NaCaCO buffer, en-block stained with saturated uranyl acetate replacement, and embedded for EM in epoxy resin (Epon 812). Ultrathin sections (∼40 nm) were cut in a Leica Ultracut R microtome (Leica Microsystem) using a Diatome diamond knife (CH-2501; Diatome Ltd) and examined at 60 kV after double-staining with uranyl acetate replacement and lead citrate with an FP 505 Morgagni Series 268D electron microscope (FEI Company) equipped with Megaview III digital camera and Soft Imaging System.

For quantitative EM analysis, micrographs at 14–18 k of magnification of non-overlapping regions were randomly collected from longitudinal sections of internal areas of EDL and soleus fibers from WT and Ho mice. See the relevant tables for additional details about sample size.

(1) The number of CRUs/area (Tables 1 and 2, column C) was evaluated on longitudinal sections and reported as an average number/100 µm². In each EM image, the orientation of CRUs (oblique/longitudinal) (Tables 1 and 2, column D) and the percentage of dyads (Tables 1 and 2, column E) were also determined.

(2) The number of mitochondria (Tables 1 and 2, column A) and mitochondria-CRUs pairs/area (Tables 1 and 2, column F) were evaluated in longitudinal sections and reported as average number/100 µm². In each EM image, the % of severely altered mitochondria over the total number of mitochondria (Tables 1 and 2, column B) was determined. Mitochondria were classified as altered when (1) the external membrane was disrupted; and/or (2) internal cristae were severely vacuolized; (3) contained myelin figures.

(3) The frequency of fibers presenting regions with the accumulation of amorphous/vesiculated material was counted and reported as the percentage of the total number of fibers.

Structural analysis of the position of the p.F4976L mutation

Analysis and graphical representation of the p.F4976L RyR1 variant were performed with the use of Pymol software (The PyMOL Molecular Graphics System, version 2.5.2; Schrödinger, LLC) or Chimera software (UCSF Chimera, production version 1.16) (Pettersen et al., 2004). The highest probability rotamers were chosen among the Dunbrack 2010 backbone-dependent rotamer library (Shapovalov and Dunbrack, 2011), and subsequently, clashes/H bonds were investigated. For the present investigation, cryo-EM-resolved protein structures with the following PDB ID were used: 5TAL (resolution of 4.6 Å) (des Georges et al., 2016; wwPDB consortium, 2019).

Statistical analysis

Statistical analysis was performed using the Origin (Pro), version 2019 software (OriginLab Corporation) using either Mann–Whitney test or the two-way analysis of variance (ANOVA) followed by the Bonferroni post-hoc test. P values smaller or equal to 0.05 were considered significant. In the case of EM quantitative analysis, mean and SEM were determined using GraphPad Prism (GraphPad Software). Statistically significant differences between groups were determined by the Student's t test (GraphPad Software) or by the χ squared test (GraphPad Software) when comparing percentages. Statistical significance was considered for values of $P < 0.05$.

Online supplemental material

Fig. S1 shows a confirmation of the presence of the p.F4976L *Ryr1* mutation in the genomic DNA, growth curves of Het mice, and frequency of male and female Ho pups. Fig. S2 shows a comparison of the total running distance. muscle grip strength, and treadmill running distance. Fig. S3 shows specific force values of EDL and soleus muscles from Het mice. Fig. S4 shows quantification of MyHC expression. Fig. S5 shows calcium release in FDB fibers from Het mice. Fig. S6 shows the analysis of transcript expression in muscles from WT and p.F4976L Ho mice. Table S1 lists the sequence of primers and target genes. Table S2 lists the antibodies and suppliers. Table S3 lists twitch and tetanic parameters for both EDL and soleus muscles of homozygous and WT mice. Table S4 shows force kinetic values of EDL and soleus muscles of Ho and WT mice. Table S5 shows the analysis of the kinetic parameters of electrically evoked Ca^{2+} transients in FDB fibers from Ho, Het, and WT mice.

Table 1. **Quantitative analyses of mitochondria and CRUs in EDL muscles**

	A	B	C	D	E	F
EDL	**No. of mitochondria/ 100 µm²**	**No. of altered mitochondria/100 µm² (%)**	**No. of CRUs/ 100 µm²**	**% of oblique/ longitudinal CRUs**	**% of dyads**	**No. of mitochondrion/ CRU pairs/100 µm²**
WT	22.8 ± 0.8	0.4 ± 0.1 (2%)	46.1 ± 0.9	4.3 ± 0.1	1.0 ± 0.9	18.6 ± 0.7
Ho	16.8 ± 0.8* (P = 2.25E-06)	2.0 ± 0.3* (12%) (P = 4.48E-06)	36.5 ± 0.9* (P = 2.42E-13)	10.5 ± 0.1* (P = 5.11E-06)	3.9 ± 0.1* (P = 0.0003)	12.3 ± 0.7* (P = 1.09E-09)

In EDL fibers from Ho mice, the frequency of mitochondria, the number of CRUs, and the number of couples mitochondrion/CRU are significantly reduced compared with WT. On the other hand, the number of damaged mitochondria, dyads (i.e., incomplete CRUs), and misoriented CRUs (oblique/longitudinal) are significantly increased compared with WT littermates. Data are shown as mean ± SEM (* P < 0.001). Samples size: 32 fibers from three WT mice, 22 fibers from three Ho littermates, five micrographs/fiber.

Results

Clinical case of the homozygous proband

The index case is a male child, born preterm at 29 wk via cesarean section for polyhydramnios to Caucasian non-consanguineous parents. He showed an intrauterine growth restriction, with a birth weight of 1,200 g. Severe hypotonia was noted soon after birth and the perinatal period was remarkable for serious respiratory distress syndrome that required mechanical ventilation and percutaneous endoscopic gastrostomy (PEG). His APGAR (appearance, pulse, grimace, activity, respiration) index was 5 at 1 min after birth and 8 at 5 min after birth. The neurological examination was characterized by persistent floppiness (floppy baby), generalized muscle weakness, hyporeactivity, absence of sucking reflex, tendon reflexes, and spontaneous motility, and minimal response of the distal and the lower limbs after painful stimulation. There were no apparent signs of cerebellar involvement, especially nystagmus, a hallmark of cerebellar dysfunction (Bodranghien et al., 2016), was absent. A general physical examination showed low-set ears, anteverted nostrils, arachnodactyly, and low-set thumbs. Moreover, bilateral cryptorchidism was evident. No anomaly was evident after a cardiological evaluation, thoracic auscultation, or abdominal palpation. CK was slightly increased (about 300 U/l). Genetic testing for spinal muscular atrophy type I (SMA-1) and myotonic dystrophy type 1 were performed but were negative. A muscle biopsy of the femoral quadriceps performed at 18 days of age showed histologic heterogeneity, including marked variability of muscle fiber size, atrophic fibers, numerous centralized nuclei, fibrosis, adipose tissue infiltration and increased connective tissue with no cores, and normal oxidative staining. Immunohistochemical analysis did not reveal significant alterations in the muscle proteins. Next-generation sequencing of the proband's complete exome revealed homozygosis for the *RYR1* gene variant c.14928C>G (p.F4976L) in exon 104. Sanger sequencing confirmed the results and identified both parents as heterozygous carriers for the same mutation. After the first months of life, his clinical picture slowly improved. During the last neurological evaluation at 4 years of age, the severe generalized hypotonia remained but he was able to independently maintain a sitting position with good head control and fair trunk control. He is able to stand using a knee-ankle-foot orthosis (KAFO) and no longer needs assisted ventilation and PEG for feeding but he is unable to walk independently. He shows a myopathic face with bilateral ptosis and mild strabismus and shows some language skill and fine motor control delays.

General phenotypic characteristics of the *Ryr1*p.F4976L mouse line

The presence of the RyR1 missense p.F4976L mutation in exon 104 was confirmed after genomic DNA and cDNA sequencing of mice from F1 generations (Fig. S1 A). The genotype of heterozygous (Het) or homozygous (Ho) mice was confirmed by digestion of the PCR-amplified cDNA fragments with *XhoI* (Fig. S1 B).

Table 2. **Quantitative analyses of mitochondria and CRUs in soleus muscles**

	A	B	C	D	E	F
	No. of mitochondria /100 µm²	**No. of altered mitochondria /100 µm² (%)**	**No. of CRUs /100 µm²**	**% of oblique/ longitudinal CRUs**	**% of dyads**	**No. of mitochondrion/ CRU pairs/100 µm²**
WT	42.5 ± 1.1	2.1 ± 0.3 (1%)	34.8 ± 1.1	4.2 ± 0.1	6.5 ± 0.1	21.6 ± 1.2
Ho	30.9 ± 1.1* (P = 8.46E-13)	3.0 ± 0.4* (10%) (P = 2.70E-07)	28.0 ± 1.0* (P = 1.19E-05)	14.9 ± 0.1* (P = 8.12E-13)	14.1 ± 0.1* (P = 3.0E-05)	12.9 ± 0.7* (P = 2.08E-09)

In soleus fibers from Ho mice, the frequency of mitochondria, the number of CRUs, and the number of couples mitochondrion/CRU are significantly reduced compared with WT. On the other hand, the number of damaged mitochondria, dyads (i.e., incomplete CRUs), and misoriented CRUs (oblique/longitudinal) are significantly increased compared with WT littermates. Data are shown as mean ± SEM. (* P < 0.001). Samples size: 28 fibers from three WT mice, 28 fibers from three Ho littermates, five micrographs/fiber.

Het and Ho mice did not show a postnatal lethal phenotype and were undistinguishable from their wild type (WT) littermates. Analysis of the growth curves starting from 3 wk of age did not reveal significant differences in body weight between male WT and Ho littermates; however, the weight of female Ho mice was significantly lower than that of WT female littermates (two-way ANOVA, Bonferroni post-hoc test) at 4 (P = 0.023), 5 (P = 0.01045), 6 (P = 0.02944), 7 (P = 0.01855), and 12 (P = 0.03819) weeks of age (Fig. 1 A). The weight of male and female Het mice was similar to that of age-matched WT littermates (Fig. S1 C). The frequency of both male and female Ho pups was significantly below the expected frequency of 25% when Ho were obtained from breeding two Het mice (Fig. 1B) and below the expected frequency of 50% when they were obtained by breeding Ho with Het mice (Fig. S1 D). Analysis of gravid uteri and fetuses harvested from Het females bred with Ho males did not show the presence of resorption sites (Fig. 1 C).

In vivo phenotype of homozygous mice

The in vivo muscle performance was initially investigated using the voluntary running wheel by calculating the average distance covered and speed run over a period of 22 days. Ho mice ran less and at a lower speed compared with WT mice (Fig. 2 A), with a mean distance covered by WT and Ho littermates, which differed significantly between the 5th and 12th night, (P = 0.02224 5th night, P = 0.01587 6th night, P = 0.01595 7th night, P = 0.02106, 8th night, P = 0.02642 9th night, P = 0.03134 10th night, P = 0.03879 11th night, and P = 0.04881 12th night), while Ho speed was lower between the 4th and 6th night (P = 0.00314 4th night, P = 0.00333 5th night, P = 0.02983 6th night) (Fig.2 A). The total distance covered at the end of the 22 days was 255 ± 12 km (n = 13), 209 ± 15 km (n = 10), and 214 ± 15 km (n = 14) for WT, Het, and Ho, respectively (Fig. 2 A and Fig. S2 A).

We also assessed muscle force by measuring forelimb grip strength over a period of 12 wk (starting from 6 wk of age). Muscles from Ho mice produced significantly less strength at 10, 15, and 16 wk of age, compared with WT littermates (Fig. 2 B) (P = 0.01457 on the 10th wk, P = 0.02407 on the 15th wk, and P = 0.02368 on the 16th wk) while grip strength of Het and WT mice was similar (Fig. S2 B). Lastly, muscle function was assessed by placing mice on a treadmill. Mice were adapted to the treadmill for two days, and on the third day the maximal running capacity and distance covered until exhaustion were calculated. Ho mice showed a 36% reduction in maximal running distance compared with WT littermates (Fig. 2 C). The mean (±SD) distance to exhaustion was 914 ± 151 m and 1,426 ± 164 m for Ho and WT, respectively (ANOVA, followed by the Bonferroni post-hoc test; P = 1.21549E-6). The distance to exhaustion for Het mice was similar to that of WT mice (of 1,387 ± 211 meters) (Fig. S2 C) and significantly different to that of Ho mice (two-way ANOVA, followed by the Bonferroni post-hoc test; P = 7.71225E-6).

Mechanical properties of EDL and soleus muscles from mutant mice

The generation of ex vivo isometric force in isolated EDL and soleus muscle from WT and transgenic mice was investigated. For each muscle, the optimal sarcomeric length was determined, and subsequently, each muscle was subjected to either a single pulse (twitch stimulation) or repeated pulses of 1-ms duration at different frequencies (Hz) (tetani) depending on the muscle being investigated. In EDL from Ho mice, the average specific twitch force was decreased by ∼36% compared with WT, resulting in a mean (±SD) specific force of 143.72 ± 37.78 and 91.99 ± 26.17 mN/mm^2 for WT (n = 11 mice) and Ho (n = 13 mice), respectively (Mann–Whitney test; P = 9.5867E-4 [Fig. 3 A and Table S3]). A significant reduction of force of EDLs from Ho mice was also observed following tetanic stimulation at all three stimulation frequencies (for 50 Hz P = 0.0143, 100 Hz P = 0.01924, and 150 Hz P = 0.02718 [Fig. 3 A and Table S3]). Soleus muscles from Ho mice showed a ∼28% decrease in the average specific twitch force; the mean ± SD specific force was 98.43 ± 16.09 (n = 11) and 70.57 ± 16.61 (n = 11) mN/mm^2 in WT and Ho, respectively (Mann–Whitney test; P = 0.00252). Intriguingly, soleus muscles from Ho mice did not show a decrease in force after tetanic stimulation at any of the stimulation frequencies (Fig. 3 B and Table S3). There were no significant differences in the kinetic parameters (HTTP, TTP, and half-relaxation time, HRT) of muscles from WT and Ho (Table S4). The twitch force developed by EDL muscles from Het mice was similar to that of WT mice (Fig. S3 A), while the force generated following tetanic stimulation of EDLs at 50, 100, and 150 Hz was reduced in Het mice (Fig. S3 A). No changes in the force developed by soleus muscles from Het mice were observed (Fig. S3 A). The decrease in force in muscles from Ho mice was not due to fiber type switching nor to atrophy as there were no changes in either parameter in muscles from Ho mice (Fig. 4 and Fig. S4).

Ca^{2+} transients in FDB fibers from WT and transgenic mice

In the next series of experiments, we investigated if the reduction of isometric force was paralleled by a diminished Ca^{2+} release during electrical stimulation of FDB fibers. Single fibers were loaded with MagFluo-4 and the changes in [Ca^{2+}] following twitch or tetanic stimulation were calculated. The peak Ca^{2+} transient (ΔF/F) in FDB from Ho mice was significantly decreased compared with that observed in FDB from WT mice; the mean (±SD) ΔF/F was 1.23 ± 0.38 (n = 69 fibers from 4 mice) and 1.04 ± 0.22 (n = 90 fibers from 6 mice) for WT and Ho, respectively (Mann–Whitney test; P = 2.16116E-4) (Fig. 5 A, top panels; and Table S5). Similarly, the peak Ca^{2+} transient generated by tetanic stimulation was significantly reduced in Ho compared with WT mice (ΔF/F was 1.20 ± 0.23, n = 66 fibers versus ΔF/F: 1.31 ± 0.36, n = 52 fibers, respectively) (Mann–Whitney test; P = 0.030) (Fig. 5 A, bottom panels; and Table S5). Analysis of the kinetic parameters of the electrically evoked Ca^{2+} transients revealed an 8% increase in the HTTP (Mann–Whitney test P = 0.026) and a 17% decrease of τ2 (Mann–Whitney test P = 0.001) (Table S5) between WT and Ho. No significant differences in the peak Ca^{2+} transients (twitch or tetanic) or in the τ values were observed between FDB from WT and Het mice (Table S5). The reduced peak calcium transient could be due to a number of modifications brought about by the presence of RyR1 mutations, including changes in the biophysical properties of the Ca^{2+} channels, reduced RyR1 content, or a combination of the two. Leaky channels are accompanied by measurable parameters

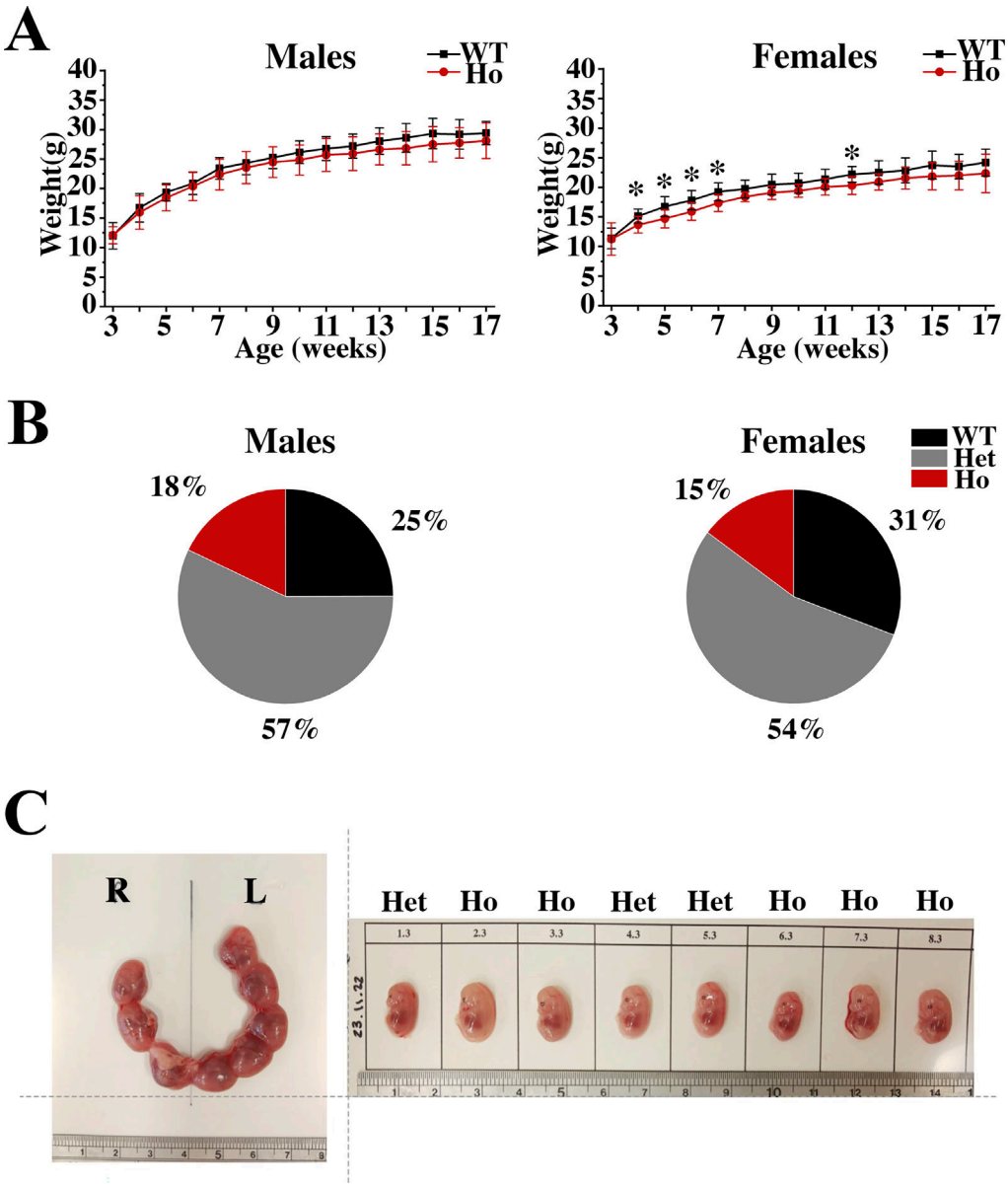

Figure 1. **Body weight and phenotypic characteristics of Ho mice. (A)** Body weight curves of WT (black squares) and Ho (red circles) over a period of 17 wk. Each symbol represents the body weight mean (±SD) of 9–12 mice. Statistical analysis was performed using two-way ANOVA, followed by the Bonferroni post-hoc test (*P < 0.05). **(B)** Genotype frequency of heterozygous × heterozygous breeding cages. Total *n* males = 593, total *n* females = 480. These frequencies are significantly different than the expected genotype frequencies for the χ2 test, with a two-tailed P value of 1.154572E-4 and 6.879268E-7, respectively. **(C)** Photograph of gravid uteri (left) and fetuses (right) harvested from Ho females bred with heterozygous males. Fetuses were harvested at 14.5 dpc and genotyped. No difference in size or appearance is noticeable between genotypes.

including smaller intracellular Ca^{2+} stores, increased channel open probability, and increased resting myoplasmic [Ca^{2+}]. The resting [Ca^{2+}] measured with the ratiometric calcium indicator fura-2 was significantly increased in FDB fibers from Ho versus WT (the mean ± SEM resting [Ca^{2+}] and was 57.3 ± 1.9 in 46 fibers from four WT mice and 83.1 ± 5.0 in 34 fibers from three Ho mice, respectively, P = 1.054E-7 [ANOVA followed by Bonferroni post hoc test]) (Fig. 5 B). Interestingly, when fibers from Ho mice were treated with 10 µM of the SOCE inhibitor BTP2, a decrease of the resting calcium was observed, reaching the level observed in fibers from WT mice. The mean (±SEM) resting [Ca^{2+}] of WT fibers treated with 10 µM BTP2 was 62.4 ± 2.4 in 41 fibers and that of Ho fibers treated with BTP2 was 57.1 ± 2.6 in 47 fibers (P values WT BTP2 versus Ho BTP2 P = 4.582E-5 and between Ho DMSO versus Ho BTP2 P = 7.888E-8). No significant changes in the resting [Ca^{2+}] of FDB fibers from Het mice were observed (Fig. S5 B). These results are compatible with the hypothesis that the homozygous expression of the p.F4976L RyR1 mutation causes the channels to become leaky, leading to reduced intracellular calcium stores, activation of calcium influx (SOCE) from extracellular space (Ríos, 2010), and increased resting [Ca^{2+}]. Consistently, the mean peak ionomycin + CPA-induced Ca^{2+} transients (ΔF/F ± SD) were 0.74 ± 0.26 and 0.27 ± 0.08 for WT (*n* = 9) and Ho (*n* = 5) mice, respectively (ANOVA

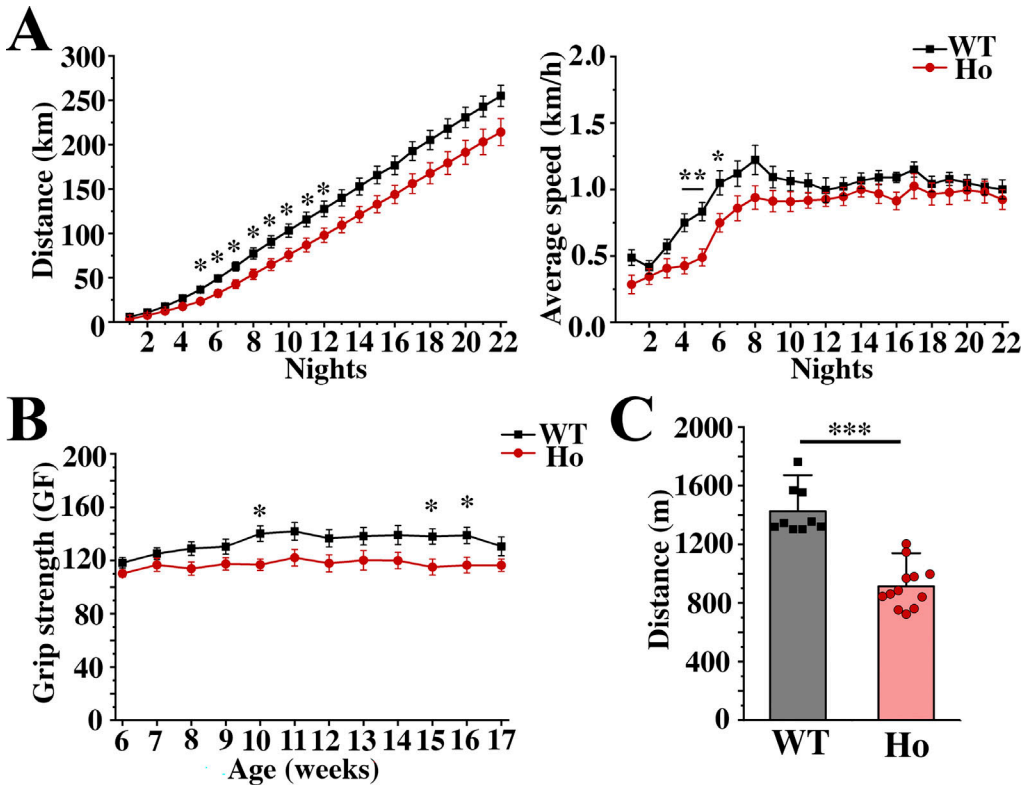

Figure 2. **In vivo muscle function is negatively affected by the presence of the Ho p.F4976L *Ryr1* mutation. (A)** Voluntary running distance and speed of WT (n = 13) and Ho (n = 14) mice (starting age = 10–13 wk) measured for a period of 22 days. Data points are expressed as mean ± SEM. Left panel shows the spontaneous locomotor cumulative distance (km) recorded during the dark phase period (5 pm–5 am). Right panel shows the average running speed (km/hour) recorded during the night phase (5 pm–5 am). Statistical analysis was performed using ANOVA, followed by the Bonferroni post hoc test. *P < 0.05. **(B)** Analysis of forelimb (anterior two paws) grip strength in WT (n = 15) and Ho (n = 15) littermates. Mice were tested once per week for a period of 12 wk starting from 6 wk of age. Five measurements for each mouse were averaged. Each point represents the mean ± SEM. ANOVA, followed by the Bonferroni post hoc test. *P < 0.05. **(C)** Comparison between the distance run by WT and Ho mice during the exhaustion treadmill test. The distance run by Ho is 36% shorter than the one run by WT littermates. Each point represents the measurement coming from a single mouse. Bars represent mean ± SD. Homozygous mice run significantly less than WT. Statistical analysis was performed using ANOVA, followed by the Bonferroni post-hoc test. ***P < 0.001.

followed by Bonferroni post-hoc test P = 0.00155) (Fig. 5 C). Moreover, the calculation of the area under the curve (AUC) confirmed the reduction of total released calcium in FDB fibers from Ho mice compared with WT, with AUC values (mean ± SEM) of WT = 179,986.75 ± 22,886.30 and Ho = 42,156.80 ± 10,054.89.

Analysis of the gating characteristics of the RyR1 channels indicates a significantly higher open probability for Ho channels at high [Ca^{2+}]; in particular, at 100 μM [Ca^{2+}], the Po were 0.4302 ± 0.0870 (n = 10) and 0.1892 ± 0.0632 (n = 10) (*P = 0.0382) for Ho and WT, respectively (Fig. 5 D). We also observed that the mutant channels are less responsive (i.e., are more open) at higher [Ca^{2+}], as the Po of Ho channels was higher in the presence of 1 mM Ca^{2+} (Po = 0.1590 ± 0.0765, n = 9) than the Po of WT channels (Po = 0.0289 ± 0.0105, n = 9) (P = 0.0191) (Fig. 5 D).

Content of proteins and transcript expression of proteins involved in ECC and SOCE in muscles from WT and transgenic mice

Next, the content of proteins involved in skeletal muscle ECC and calcium homeostasis of EDL and soleus muscle was investigated (Fig. 6, A and B). We observed a 21% and 10% reduction of RyR1 content in EDL and soleus muscles from Ho mice (Mann–Whitney test; respectively, P = 0.04476 and P = 0.03656; however, this was not accompanied by a change in the *Ryr1* transcript level (Fig. S6, A and B). Of note, *Stim1* transcript levels were increased in EDL from Ho mice compared with WT (Fig. S6, P = 0.0313, Mann–Whitney). The levels and content of other transcripts and proteins were similar in muscles from WT and Ho (Fig. 6).

Additionally, we analyzed the biochemical characteristics of extraocular muscles (EOMs) from Ho mice. This is because some patients, particularly those carrying recessive mutations including our index patient, showed involvement of EOMs leading to ophthalmoplegia or ptosis (Amburgey et al., 2013; Abath Neto et al., 2017). In EOMs from Ho mice, the RyR1 protein level was significantly reduced by 22% compared with WT (Mann–Whitney test; P = 0.01987) (Fig. 6 C). Furthermore, MyHC13 was significantly reduced by ∼50% in EOMs from Ho mice (Mann–Whitney test; P = 0.00822) (Fig. 6 C).

Ultrastructural analysis

Skeletal muscle fibers from adult WT mice are characterized by a regular transverse pale-dark striation due to well-aligned

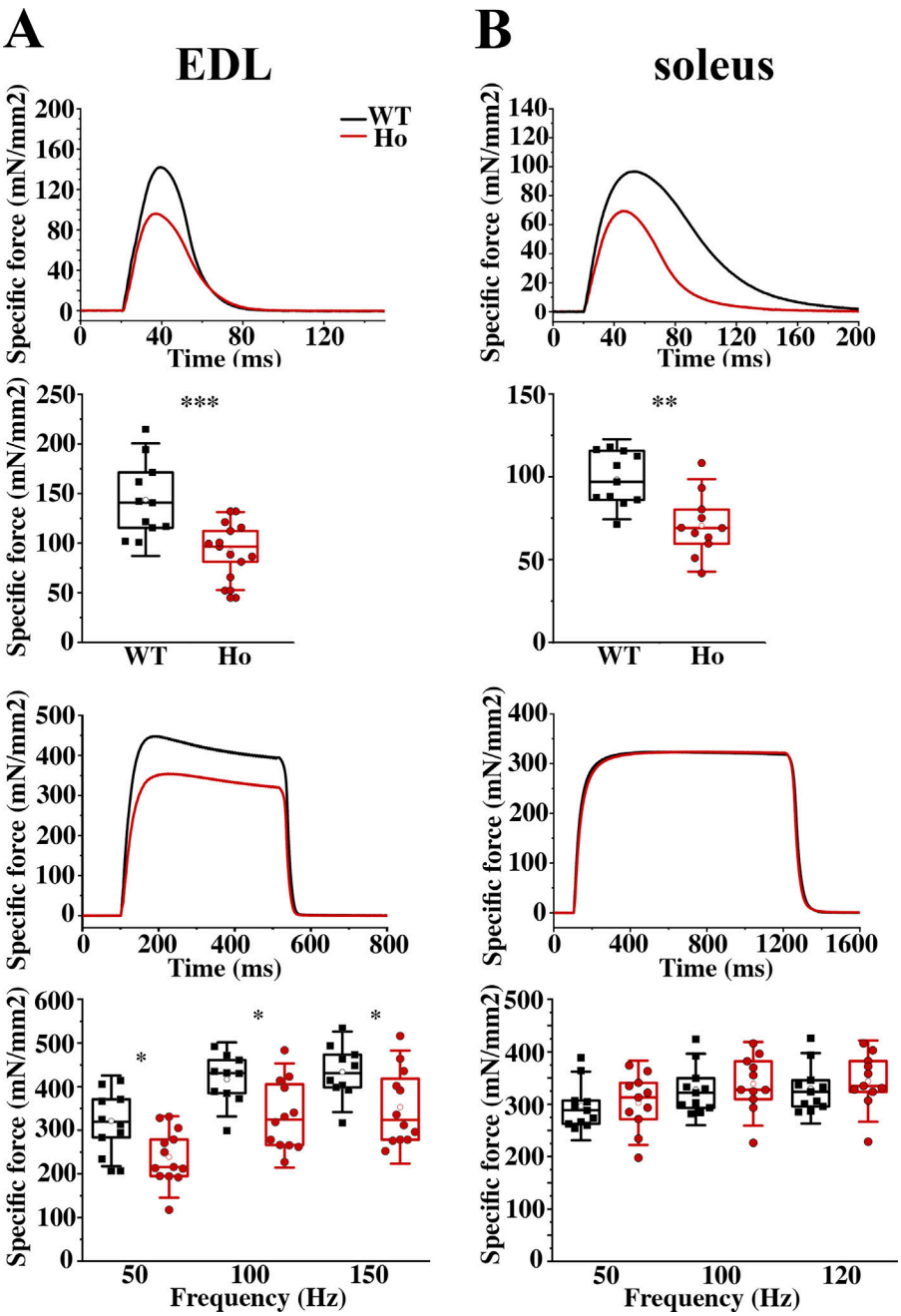

Figure 3. **The mechanical properties of muscles are impacted by the presence of the homozygous p.F4976L mutation. (A)** Representative traces and force plots of EDL muscles during either twitch (upper panels) or tetanic (lower panels) stimulation. **(B)** Representative traces and force plots of soleus muscles during twitch (upper panels) and tetanic (lower panels) stimulation. Boxes show 25 and 75 percentiles. Inner line shows median, whiskers show ±SD, each symbol represents values from a single mouse. Mann–Whitney test, *P < 0.05, **P < 0.01, ***P < 0.001.

sarcomeres (Fig. 7, A and B, panels a). These structures are delimited by two Z lines, and the calcium release units (CRUs) are uniformly distributed on both sides of the Z line (Fig. 7 A, panels a and d), approximately placed at the A–I band transition when sarcomeres are relaxed. Often CRUs are in close proximity to a mitochondrion to form a functional couple (Boncompagni et al., 2009). One longitudinal mitochondrion is marked with an "m" in Fig. 7 B, panel a. In Ho mice, 35% of all EDL fibers and 20% of all soleus fibers contain focal areas of myofibrillar degeneration (Fig. 7 A, panels b, c, e; and f. Fig. 7 B, panels b and c). The pale–dark striation is compromised in some regions: at higher magnification, these areas are characterized by an accumulation of various materials (apparently amorphous in EDLs and also vesiculated in soleus muscles), possibly resulting from damaged sarcotubular and mitochondrial membranes. These areas are not present in EDL and soleus fibers from WT mice. The sarcomeres placed next to these areas may also have altered/missing/misaligned Z lines (asterisks in Fig. 7 A, panel c; inset in Fig. 7 B, panel b). Moreover, it seems that the areas of degeneration are apparently enclosed by elongating transverse tubules (TT) that initially incorporate mitochondria (small arrows in Fig. 7 A, panel f; small arrows in insets of Fig. 7 B, panels b and c). These TTs originate from CRUs which appear to be often misoriented (oblique/longitudinal) and abnormally shaped (see inset in Fig. 7 B, panel b), i.e., they are formed by only two elements (dyads).

Quantitative analyses of mitochondria, CRUs, and their reciprocal association indicate that both in EDL and soleus muscles from Ho mice all these parameters are significantly reduced

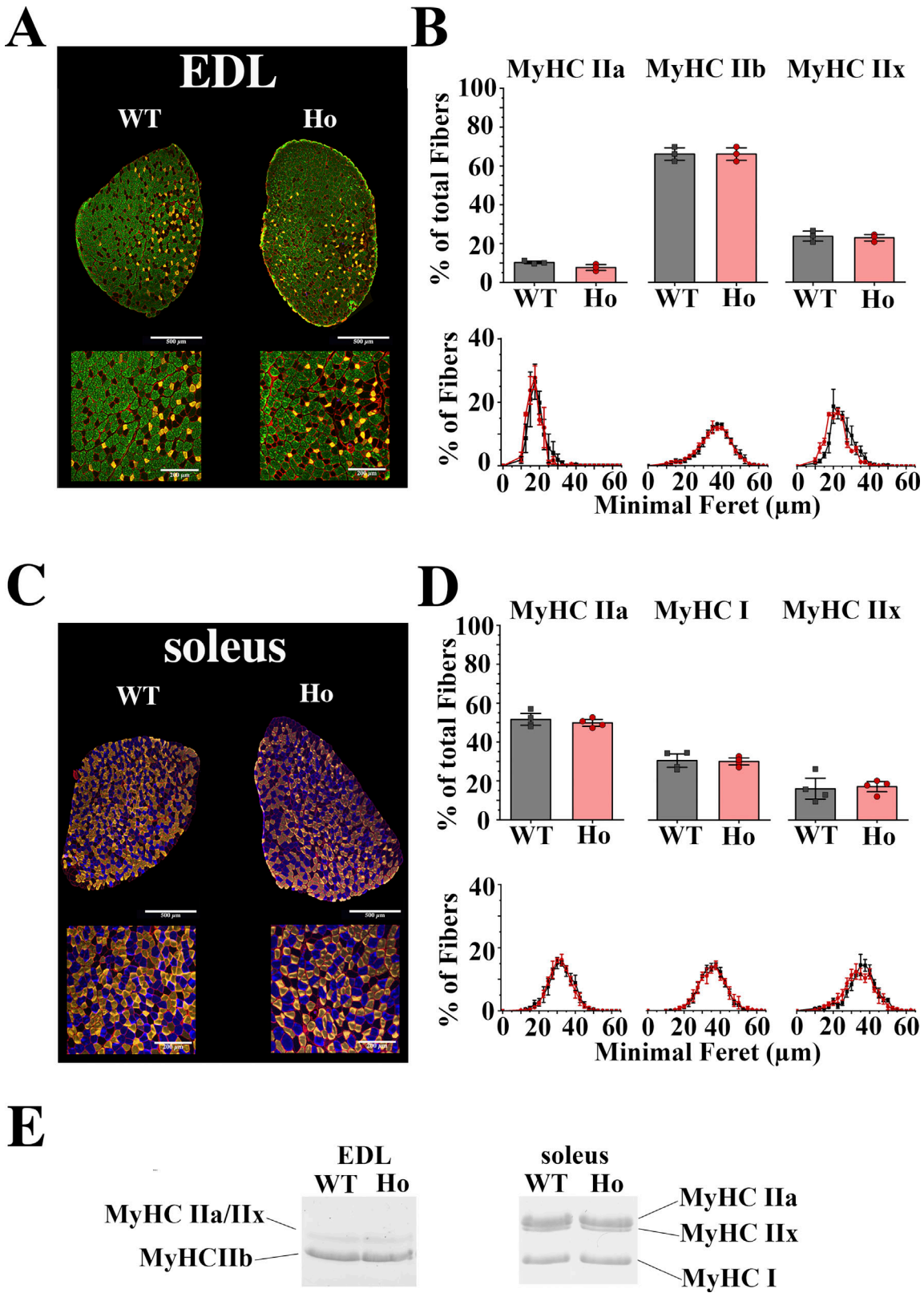

Figure 4. **EDL and soleus from homozygous mice do not show any sign of fiber type switch or atrophy. (A and C)** Representative images of EDL and soleus muscle sections from WT and Ho littermates, scale bars 500 µm (upper panels) and 200 µm (lower panels). Muscle sections were stained with specific antibodies to detect MyHC isoforms. Fibers characterized by the presence of the MyHC IIA isoform are shown in yellow, while those containing MyHC IIB are shown in green, and those containing MyHC I are shown in blue; unstained (black) fibers are MyHC IIx containing fibers. The fiber membrane (stained by laminin) is shown in red. **(B and D)** Bar plots showing specific fiber distribution (bars show mean ± SEM) and minimal Feret distribution of both EDL and soleus muscles. Each symbol represents the mean ± SEM value from a single mouse. **(E)** Representative Coomassie Blue staining of MyHC isoforms in EDL and soleus muscles. No difference was found in MyHC isoform expression between genotypes.

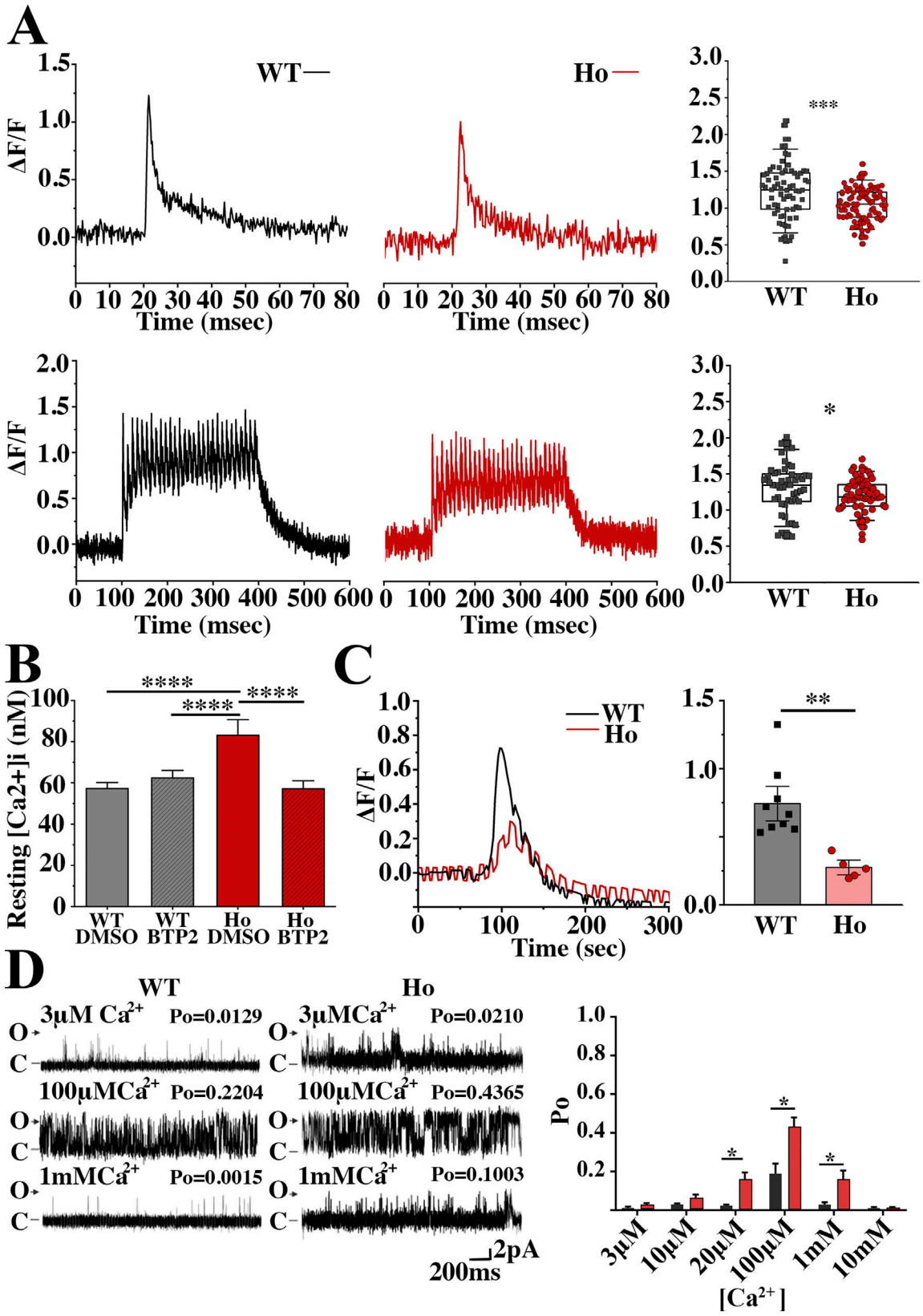

Figure 5. **Electrically evoked calcium transients and resting [Ca^{2+}] in FDB fibers and single channel recordings. (A)** Representative traces of MagFluo-4 fluorescence changes in single FDB fibers from WT (*n* = 4 mice) and Ho (*n* = 6 mice) after twitch and tetanic stimulation (top and lower panels, respectively). Statistical analysis was performed using the Mann–Whitney test (*P < 0.05; ***P < 0.001). Each symbol represents the value from a single fiber. **(B)** Analysis of the resting [Ca^{2+}] levels (Fura-2 fluorescent ratio) in FDB fibers from WT (*n* = 4 mice) and Ho littermates (*n* = 3 mice) (ANOVA, followed by the Bonferroni post-hoc test **P < 0.001). **(C)** Representative trace and bar plots of total calcium store release after the application 10 µM ionomycin + 30 µM CPA and 100 µM La^{3+}

to FDB fibers. Right panel: Each symbol represents the mean value from 2–4 fibers from a single mouse. Bars show means and error bars show SEM. Statistical analysis was performed using Mann–Whitney test (**P < 0.001). **(D)** Left panel: Representative single-channel RyR1 current fluctuations from WT (lefthand panels) and Ho (righthand panels) mice in the presence of 3 μM Ca^{2+} (top traces), 100 μM Ca^{2+} (middle traces), and 1 mM Ca^{2+} (bottom traces**). O and C indicate the open and closed channel levels, respectively. The Po value above each trace refers to the average Po determined over a 3-min period for that channel. Right panel: Bar plot of Po of WT and Ho channels when at different concentrations of Ca^{2+}. Ho channels show higher opening probabilities at 20 μM, 100 μM, and 1 mM calcium.

compared with muscles from WT mice (Tables 1 and 2, columns A, C, and F). Moreover (1) the number of damaged mitochondria (Tables 1 and 2, columns B) and (2) the percentage of dyads and misoriented CRUs (i.e., oblique/longitudinal) (Tables 1 and 2, columns D and E) are all significantly increased in EDL and soleus muscles from Ho mice compared with muscles from WT littermates. In particular, while we should not directly compare results in EDL with results in soleus muscles, we noticed that while the percentage of altered mitochondria in EDL and soleus (12% and 10%, respectively) is not significantly different, the percentage of dyads shows a 3.9-fold increase in Ho versus WT EDL, but only a 2.2-fold increase in Ho versus WT soleus (Tables 1 and 2, columns B and E).

Discussion

Here, we investigated the phenotype of a mouse model carrying the recessive missense mutation p.F4976L in the RyR1, which is isogenic to that present in the RyR1 of a severely affected child suffering from a recessive form of RyR1-CM myopathy. The expression of the recessive missense mutation causes an average 22% and 10% reduction of the RyR1 protein content in the total homogenate from fast and slow muscles, respectively. We also found that the RyR1 protein content was reduced in the total homogenate of EOM, confirming the frequent EOM involvement in patients with recessive RyR1 myopathies, including our index case. The decrease of the skeletal muscle RyR1 content is associated with a decrease in the (1) in vivo muscle performance and (2) ex vivo muscle strength, which occurs mainly in fast-twitch EDL muscles. The muscle phenotype of the murine model is overall milder compared with that present in the affected child during the early phases of postnatal development and up to 4 years of age. Although at this point in time we do not have clear explanations for these results, we believe that such discrepancies might be due to (1) fundamental differences between human and murine species; (2) the fact that the affected child was also born prematurely and this event, in addition to the RyR1 mutation, might have jeopardized the motor milestones during postnatal development; and (3) stronger epigenetic changes in the skeletal muscles of the affected child because of lower muscle activity resulting from a poor ability to deambulate (Damal Villivalam et al., 2021). Importantly, the same mutation has previously been reported in several patients affected by a severe form of CM with dysmorphic features and dysphagia. In the first description, Astrea et al. (2015) reported two affected sisters with floppiness, skeletal deformities, respiratory difficulties, and delayed milestones who carried the homozygous c.14928C>T *RYR1* (p.F4976L) missense mutation together with a *SLC7A9* mutation (linked to cystinuria type B). The second report by Laforgia et al. (2018) describes a severely affected child (who died at 1 month of age) born preterm at 34 wk for polyhydramnios, severe hypotonia, who carried the hypomorphic c.4094del G mutation + c.14928C>G (p.F4976L). More recently, Mauri et al. (2021) described two severely affected cousins carrying the c14928C>G substitution. These results support the causative role of the homozygous p.F4976L RyR1 mutation and the severe congenital myopathy in humans. In agreement with a previous study (Elbaz et al., 2020), here we show the biallelic expression of the missense mutation in the RyR1 gene is associated with a milder muscle phenotype compared with that occurring in the presence of a hypomorphic allele or in the presence of monoallelic expression, emphasizing the importance of the RyR1 gene dosage in determining the muscle phenotype.

On a structural level, the rabbit p.F4975L RyR1 mutation (corresponding to the human F4976L) is located within the CTD domain (dark red domain in Fig. 8 A left). In Fig. 8 A, the right panel shows a zoom of the region surrounding the mutation, and the 4975 phenylalanine is depicted in cyan. This domain is adjacent to ATP binding (green), Zn^{2+}-binding (violet), Ca^{2+}-binding (yellow), and caffeine-binding (magenta) sites. From a structural point of view, the substitution of a phenylalanine (F) to a leucine (L) does not affect the overall amino acid charges but could have a steric effect, and the substitution is predicted to participate in possible clashes with F4968 and S4965 (Fig. 8 B).

Muscle phenotype associated with the biallelic expression of the RyR1 p.F4976L mutation

Here, we found a poor performance of the F4976L RyR1 mutant mice on the exhaustion treadmill assay, a result indicating an increased fatigability of both fast and slow twitch muscles in Ho mice. In addition, we found that the muscle phenotype of fast EDL muscles is impacted to a greater extent than that of slow-twitch soleus muscles in the ex vivo muscle strength assay. A number of explanations may account for the different muscle phenotypes between fast and slow twitch muscles. Although fast and slow twitch muscles share basic functional and metabolic mechanisms, there is a great deal of data showing functional and molecular heterogeneity between the two different fiber types. In particular, the functional and structural heterogeneities impinge on the calcium homeostasis tool kit whereby fast and slow twitch muscles display differences not only in the kinetics of the calcium transients leading to muscle contraction but also in resting calcium concentration (Baylor and Hollingworth, 2012). Fibers isolated from soleus muscles have higher resting calcium concentrations compared with fast twitch fibers (Elbaz et al., 2020), a result consistent with higher calcium influx reported in fatigue-resistant slow twitch muscle fibers (Carrell et al., 2016). It is tempting to speculate that slow-twitch fibers may

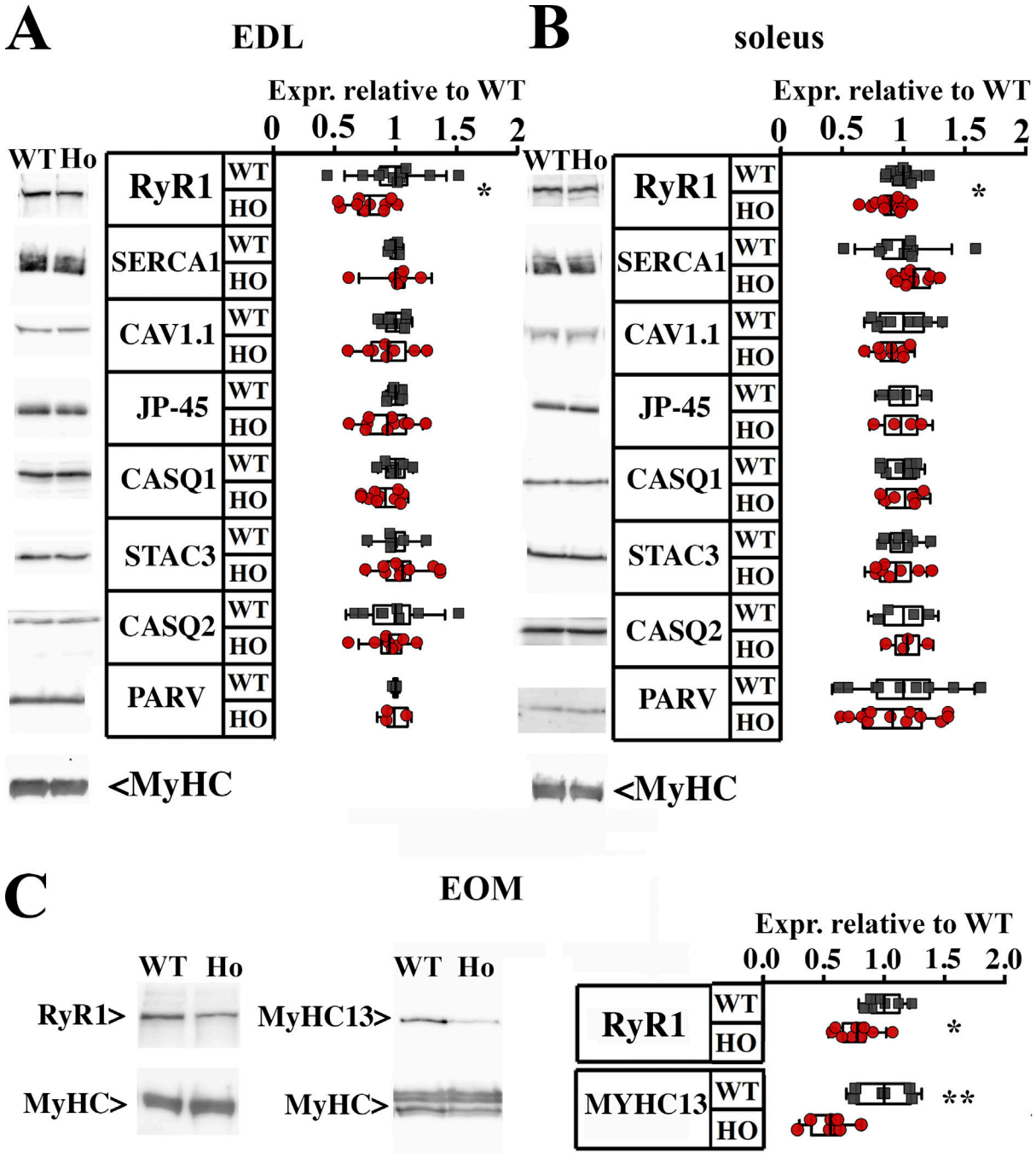

Figure 6. **Biochemical analysis of EDL, soleus, and EOM muscles. (A and B)** Western blot analysis of the major excitation–contraction proteins in EDL and soleus muscles from WT and Ho adult mice (Mann–Whitney test; *P < 0.05). The representative immunopositive bands are shown on the left of each panel. In the box plots shown in panels A and B, each symbol represents the value obtained from a single mouse, normalized on total MyHC. Boxes express 25 and 75 percentiles. Central line shows the mean. Whiskers show ±SD. **(C)** Western blots of RyR1 and MyHC13 immunoreactivity in extraocular muscles of WT and Ho mice. RyR1 is decreased by 22% in EOMs from Ho mice compared to WT (Mann–Whitney test, *P < 0.05; **P < 0.01). Boxes show 25 and 75 percentiles. Inner line shows mean, whiskers show ±SD. Each symbol represents the value from one mouse.

better handle higher resting calcium concentrations because their oxidative metabolism is crucial for the production of ATP, which ultimately supports the activity of the calcium pump, an event of paramount importance in maintaining proper myoplasmic calcium homeostasis. The expression of the p.F4976L mutant RyR1s leads to an increase of both calcium leak from the SR and of the resting calcium concentration. We believe that the damage, if any, associated with the abnormal increase of calcium leak and resting calcium concentration induced by the expression of the p.F4976L RyR1 mutation is less relevant in soleus slow muscle because soleus muscles express higher levels of heat shock proteins (Eckhardt et al., 2023), which activate cellular reparative processes aimed at counterbalancing damaging events induced by the RyR1 mutations. We speculate that the

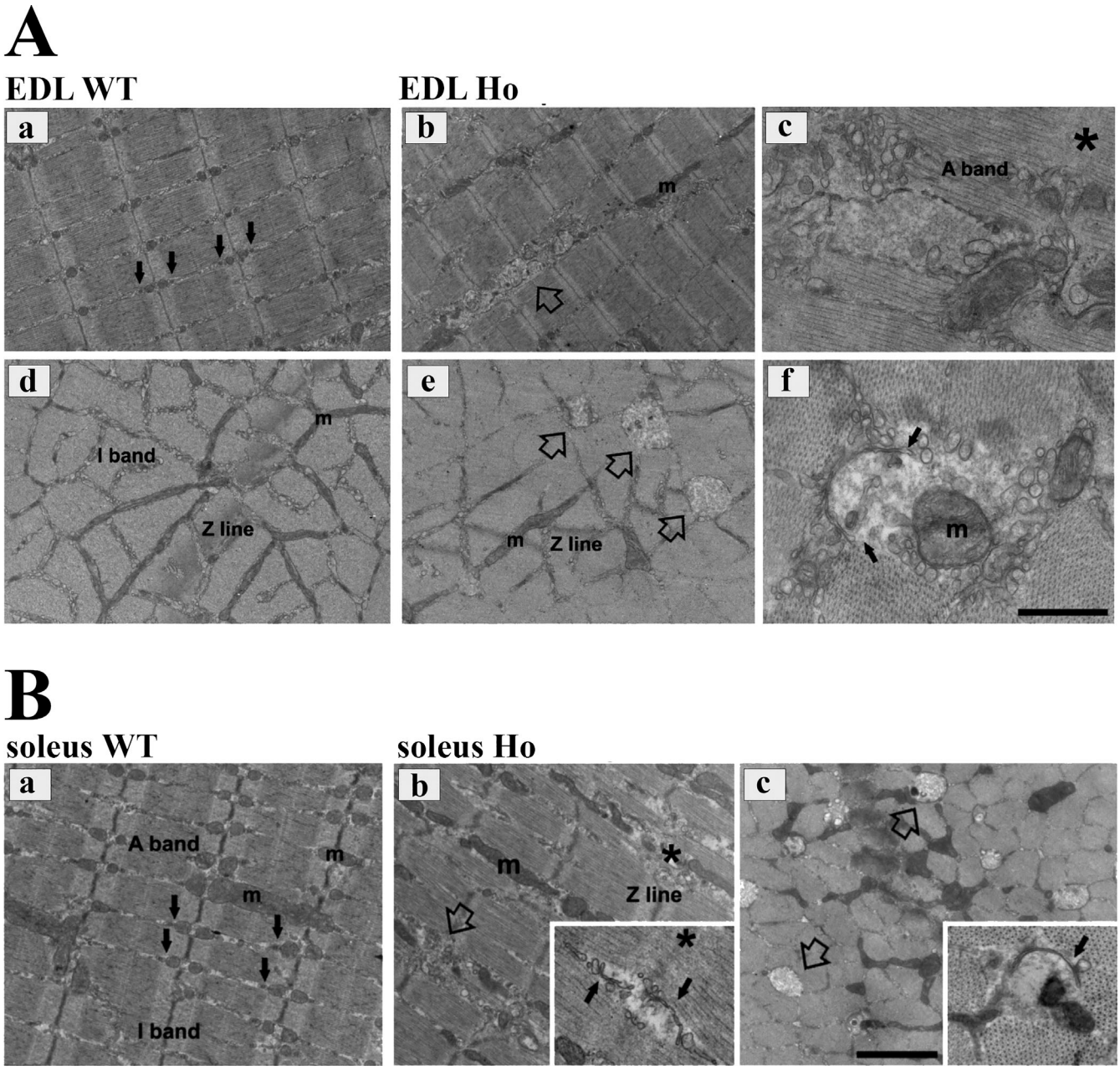

Figure 7. **Electron microscopy (EM) analysis of EDL and soleus muscles from WT and Ho mice. (A)** Panels a, b, d, and e show representative longitudinal (a and b) and transversal (d and e) EM images at low-medium magnifications of EDL fibers from WT (a and d) and Ho (b and e) mice. In a the typical pale–dark striation of EDL fibers from WT mice is shown and black arrows point to functional couples (or pairs) formed by a calcium release unit (CRU, also called triad because it is formed by a transverse tubule and two terminal cisternae of sarcoplasmic reticulum) and a mitochondrion, placed on the triad side next to the Z line. In d, mitochondria (m) are also well visible at the I band of sarcomeres, next to the Z line. In b and e, empty arrows point to focal areas of myofibrillar degeneration in muscles from Ho mice. Panels c and f: Higher magnification images from Ho mice showing the amorphous material replacing the myofibrillar components. Asterisk in c highlights a missing Z line at the I band. In f, the focal area of degeneration is surrounded by elongations of transverse tubules (TT) originating from CRUs (black arrows) and is in close proximity to an altered mitochondrion (m). Scale bars in panels a, b, d, and e, 2 µm; c and f, 500 nm. **(B)** Panels a, b, and c show representative longitudinal (a and b) and transversal (c) EM images at low-medium magnification of soleus fibers from WT (a) and Ho (b and c) mice. In a, the typical pale–dark striation of soleus fibers in WT mice is shown; black arrows point to CRUs, often coupled to mitochondria (m) to form functional couples (or pairs). In soleus muscles, mitochondria (m) are also typically found at the A band of sarcomeres. In Ho mice, the ultrastructure of fibers is characterized by presence of myofibrils not always well aligned, altered, or disrupted Z lines (asterisks in panel b), and regions with accumulating material (empty arrows in panel b and c). Insets in panels b and c: images at higher magnification showing initial myofibrillar degeneration next to elongations of TT originating from incomplete and/or misoriented CRUs (black arrows). Scale bars in panels a, b, and c, 2 µm; inset in b and c, 1 µm.

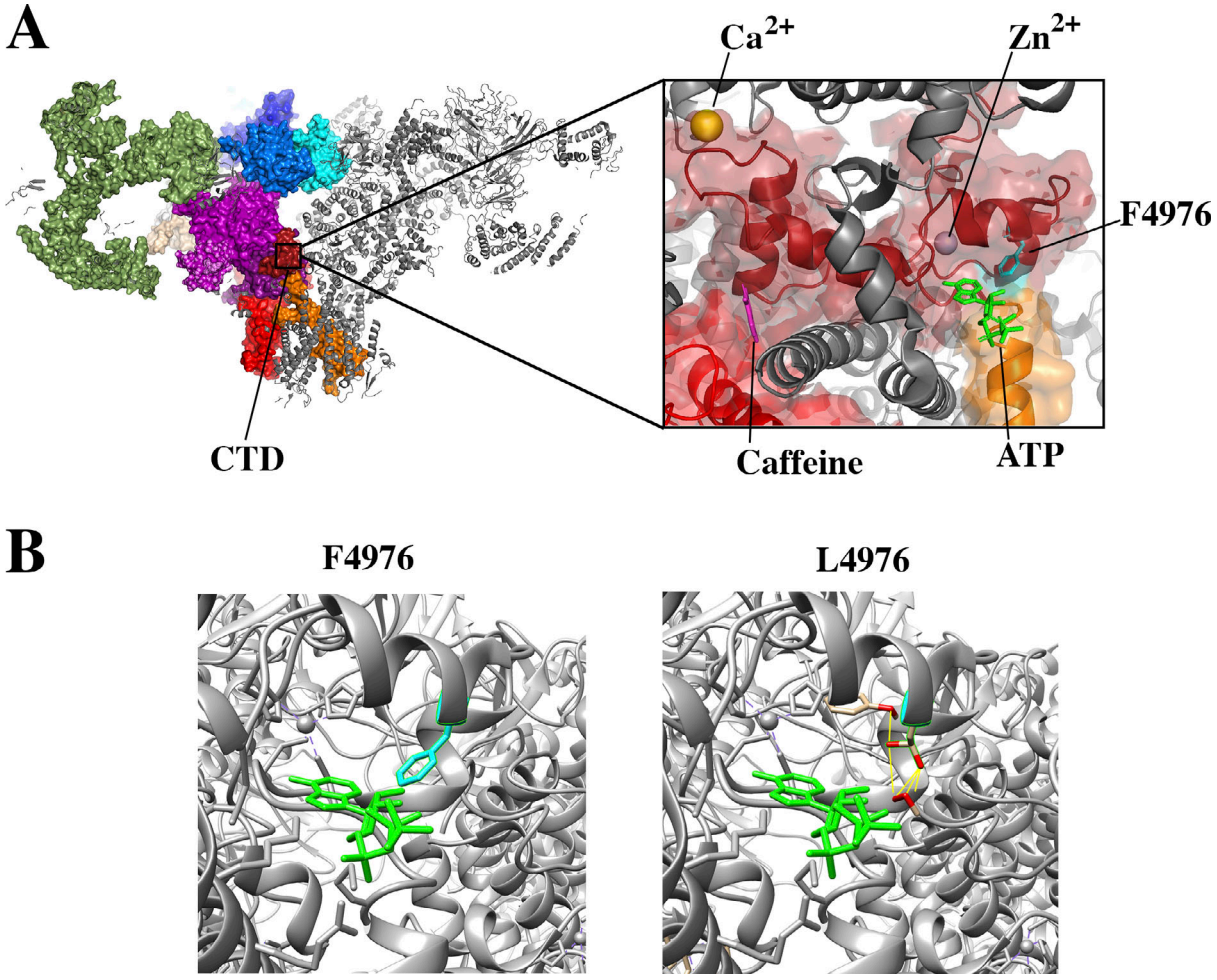

Figure 8. **Position of the p.F4976L mutation in the RyR1 structure. (A)** The left panel shows a schematic representation of a longitudinal section of the RyR1 and its subdomains. The F4976L mutation (corresponding F4975L in the rabbit structure) is present within the CTD domain (dark red). The right panel shows a zoomed-in view of the region surrounding the mutation (shown in cyan). The right panel also shows the location of a neighboring ATP binding domain (green), Zn^{2+}-binding domain (violet), Ca^{2+}-binding domain (yellow), and caffeine-binding domain (magenta). **(B)** The F4976L (F4975 in the rabbit structure) mutation is close to the ATP binding site. The substitution of the phenylalanine (F) residue with a leucine (L) residue does not affect the overall charges, but could rather cause a steric modification. The leucine residue could participate in possible clashes with the neighboring F4968 and S4965. The analyzed structure has the PDB ID code 5TAL.

reparative mechanisms of soleus muscles in Ho mice perform more efficiently, and this may also explain the less severe structural alterations observed in soleus muscles compared with EDL muscles. Indeed, EM analysis showed that while the percentage of altered mitochondria in EDL and soleus (12% and 10%, respectively) is not significantly different, the percentage of dyads shows a 3.9-fold increase in Ho versus WT EDL but only a 2.2-fold increase in Ho versus WT soleus. These structural differences in addition to a lower decrease of the RyR1 protein content in soleus fibers may explain why soleus muscles from p.F4976L RyR1 mice are functionally less affected compared with fast-twitch muscles.

As to the involvement of EOMs in patients with AR-RYR1 myopathies (Amburgey et al., 2013; Abath Neto et al., 2017), in a previous study characterizing EOM function in a mouse model carrying compound heterozygous *Ryr1* mutations (dHT mice), we reported that the presence of recessive *Ryr1* mutations is accompanied not only by a reduction in RyR1 protein content but also by significant changes in the biochemical composition of this group of specialized muscles (Eckhardt et al., 2020, 2023). Two of the proteins whose expression levels are severely reduced in dHT mice are RyR1 and MyHC-EO (Myh13). We hypothesize that the reduced expression of RyR1 and MyHC-EO, the latter being a "superfast MyHC isoform" (Wieczorek et al., 1985; Schiaffino et al., 2015) is an underlying cause of ptosis and ophthalmoplegia. In line, EOM from Ho mice showed significantly lower levels of RyR1 and MyHC-Eo (Myh13), and our index case exhibits EOM involvement and ophthalmoplegia.

Gene-dosage effect of recessive *Ryr1* mutations

Comparison of heterozygous RyR1 p.F4976L mice with age-matched homozygous RyR1 p.F4976L mice shows that the former exhibit a muscle phenotype that is virtually indistinguishable from that of WT mice; namely, we did not find significant differences, neither in vivo muscle nor ex vivo muscle strength (see the supplemental figures). Interestingly, the lack

of any obvious effect on muscle phenotype correlates with similar expression levels of the RyR1 protein in total muscle homogenates of Het RyR1 p.F4976L mice with that of WT littermates. Our data are consistent with the idea that intracellular pathways activated by the heterozygous expression of the RyR1 p.F4976L mutation are not identical to those activated by the homozygous expression of the same mutation. In particular, it appears that the higher dosage of the mutant allele accounts for the decrease of RyR1 expression and the appearance of a relatively mild muscle phenotype in the mice carrying homozygous *Ryr1* mutations. This conclusion is consistent with our previous data obtained comparing the muscle phenotype of compound heterozygous RyR1Q1970fsX16+A4329D mice with aged-matched homozygous mice carrying the p.A4391D RyR1 mutation (Elbaz et al., 2019b, 2020). The analysis of mice with biallelic expression of the missense RyR1 p.A4329D mutation shows that their muscle phenotype is milder than that of mice expressing the monoallelic p.A4391D mutation in a compound heterozygous genetic background (RyR1Q1970fsX16+A4329D). Such a finding reinforces the idea that the genetic makeup of patients with recessive RYR1-CM strongly influences the muscle phenotype. The results of this study raise important findings that should be taken into consideration for the development of therapeutic approaches aimed at rescuing RyR1 expression and function, as well as the weak muscle phenotype to treat congenital myopathies linked to recessive *RYR1* mutations.

Data availability

All data are available in the article itself and in its supplementary materials.

Acknowledgments

Eduardo Ríos served as editor.

This work was supported by a grant from the Schweizerischer Nationalfonds zur Förderung der Wissenschaftlichen Forschung (310030_184765, 310030_212192), and grants from SwissLife (projects 1206 and 1251) and the RyR1 Foundation. This work was also supported by a grant from Italian Telethon ONLUS GGP19231 to F. Protasi.

Author contribution: Conceptualization: S. Benucci, A. Ruiz, M. Franchini, S. Treves, and F. Zorzato; Data curation: S. Benucci, A. Ruiz, M. Franchini, L. Ruggiero, D. Zoppi, R. Sitsapesan, C. Lindsay, P. Pelczar, L. Pietrangelo, F. Protasi, S. Treves, and F. Zorzato; Formal Analysis: S. Benucci, A. Ruiz, M. Franchini, L. Ruggiero, D. Zoppi, R. Sitsapesan, C. Lindsay, L. Pietrangelo, S. Treves, and F. Zorzato; Investigation: S. Benucci, A. Ruiz, M. Franchini, L. Ruggiero, D. Zoppi, R. Sitsapesan, C. Lindsay, L. Pietrangelo, F. Protasi, S. Treves, and F. Zorzato; Funding acquisition: S. Benucci, S. Treves, and F. Zorzato; Methodology: S. Benucci, A. Ruiz, M. Franchini, L. Ruggiero, D. Zoppi, R. Sitsapesan, C. Lindsay, L. Pietrangelo, S. Treves, and F. Zorzato; Project administration: S. Benucci, A. Ruiz, M. Franchini, S. Treves, and F. Zorzato; Resources: R. Sitsapesan, P. Pelczar, S. Treves, and F. Zorzato; Supervision: F. Protasi, S. Treves, and F. Zorzato; Validation: S. Benucci, A. Ruiz, M. Franchini, L. Ruggiero, C. Lindsay, L. Pietrangelo, F. Protasi, S. Treves, and F. Zorzato; Writing—original draft: S. Benucci, L. Ruggiero, C. Lindsay, L. Pietrangelo, S. Treves, and F. Zorzato: Writing—review & editing: S. Benucci, A. Ruiz, M. Franchini, L. Ruggiero, C. Lindsay, L. Pietrangelo, F. Protasi, S. Treves, and F. Zorzato.

Disclosures: The authors declare no competing interests exist.

Submitted: 14 September 2023
Revised: 20 December 2023
Accepted: 9 February 2024

References

Abath Neto, O., C.A.M. Moreno, E. Malfatti, S. Donkervoort, J. Böhm, J.B. Guimarães, A.R. Foley, P. Mohassel, J. Dastgir, D.X. Bharucha-Goebel, et al. 2017. Common and variable clinical, histological, and imaging findings of recessive RYR1-related centronuclear myopathy patients. *Neuromuscul. Disord.* 27:975–985. https://doi.org/10.1016/j.nmd.2017.05.016

Agrawal, A., G. Suryakumar, and R. Rathor. 2018. Role of defective Ca^{2+} signaling in skeletal muscle weakness: Pharmacological implications. *J. Cell Commun. Signal.* 12:645–659. https://doi.org/10.1007/s12079-018-0477-z

Amburgey, K., A. Bailey, J.H. Hwang, M.A. Tarnopolsky, C.G. Bonnemann, L. Medne, K.D. Mathews, J. Collins, J.R. Daube, G.P. Wellman, et al. 2013. Genotype-phenotype correlations in recessive RYR1-related myopathies. *Orphanet J. Rare Dis.* 8:117. https://doi.org/10.1186/1750-1172-8-117

Astrea, G., I. Munteanu, D. Cassandrini, S. Lillis, R. Trovato, E. Pegoraro, G. Cioni, E. Mercuri, F. Muntoni, and R. Battini. 2015. A diagnostic dilemma in a family with cystinuria type B resolved by muscle magnetic resonance. *Pediatr. Neurol.* 52:548–551. https://doi.org/10.1016/j.pediatrneurol.2015.01.018

Baylor, S.M., and S. Hollingworth. 2012. Intracellular calcium movements during excitation-contraction coupling in mammalian slow-twitch and fast-twitch muscle fibers. *J. Gen. Physiol.* 139:261–272. https://doi.org/10.1085/jgp.201210773

Bodranghien, F., A. Bastian, C. Casali, M. Hallett, E.D. Louis, M. Manto, P. Mariën, D.A. Nowak, J.D. Schmahmann, M. Serrao, et al. 2016. Consensus paper: Revisiting the symptoms and signs of cerebellar syndrome. *Cerebellum.* 15:369–391. https://doi.org/10.1007/s12311-015-0687-3

Boncompagni, S., A.E. Rossi, M. Micaroni, S.L. Hamilton, R.T. Dirksen, C. Franzini-Armstrong, and F. Protasi. 2009. Characterization and temporal development of cores in a mouse model of malignant hyperthermia. *Proc. Natl. Acad. Sci. USA.* 106:21996–22001. https://doi.org/10.1073/pnas.0911496106

Calderón, J.C., P. Bolaños, S.H. Torres, G. Rodríguez-Arroyo, and C. Caputo. 2009. Different fibre populations distinguished by their calcium transient characteristics in enzymatically dissociated murine flexor digitorum brevis and soleus muscles. *J. Muscle Res. Cell Motil.* 30:125–137. https://doi.org/10.1007/s10974-009-9181-1

Calderón, J.C., P. Bolaños, and C. Caputo. 2014. The excitation-contraction coupling mechanism in skeletal muscle. *Biophys. Rev.* 6:133–160. https://doi.org/10.1007/s12551-013-0135-x

Carrell, E.M., A.R. Coppola, H.J. McBride, and R.T. Dirksen. 2016. Orai1 enhances muscle endurance by promoting fatigue-resistant type I fiber content but not through acute store-operated Ca^{2+} entry. *FASEB J.* 30:4109–4119. https://doi.org/10.1096/fj.201600621R

Castro, B., and S. Kuang. 2017. Evaluation of muscle performance in mice by treadmill exhaustion test and whole-limb grip strength assay. *Bio Protoc.* 7:e2237. https://doi.org/10.21769/BioProtoc.2237

Colquhoun, D., and F.J. Sigworth. 1995. Fitting and statistical analysis of single-channel records. *In* Single-Channel Recording. E. Neher, editors B. Sakmann, Springer, Boston, MA. https://doi.org/10.1007/978-1-4419-1229-9_19

Damal Villivalam, S., S.M. Ebert, H.W. Lim, J. Kim, D. You, B.C. Jung, H.H. Palacios, T. Tcheau, C.M. Adams, and S. Kang. 2021. A necessary role of DNMT3A in endurance exercise by suppressing ALDH1L1-mediated oxidative stress. *EMBO J.* 40:e106491. https://doi.org/10.15252/embj.2020106491

Delezie, J., M. Weihrauch, G. Maier, R. Tejero, D.J. Ham, J.F. Gill, B. Karrer-Cardel, M.A. Ruegg, L. Tabares, and C. Handschin. 2019. BDNF is a mediator of glycolytic fiber-type specification in mouse skeletal muscle. *Proc. Natl. Acad. Sci. USA*. 116:16111–16120. https://doi.org/10.1073/pnas.1900544116

des Georges, A., O.B. Clarke, R. Zalk, Q. Yuan, K.J. Condon, R.A. Grassucci, W.A. Hendrickson, A.R. Marks, and J. Frank. 2016. Structural basis for gating and activation of RyR1. *Cell*. 167:145–157.e17. https://doi.org/10.1016/j.cell.2016.08.075

Dirksen, R.T., and G. Avila. 2004. Distinct effects on Ca^{2+} handling caused by malignant hyperthermia and central core disease mutations in RyR1. *Biophys. J.* 87:3193–3204. https://doi.org/10.1529/biophysj.104.048447

Dowling, J.J., H. D Gonorazky, R.D. Cohn, and C. Campbell. 2018. Treating pediatric neuromuscular disorders: The future is now. *Am. J. Med. Genet. A*. 176:804–841. https://doi.org/10.1002/ajmg.a.38418

Eckhardt, J., C. Bachmann, S. Benucci, M. Elbaz, A. Ruiz, F. Zorzato, and S. Treves. 2020. Molecular basis of impaired extraocular muscle function in a mouse model of congenital myopathy due to compound heterozygous Ryr1 mutations. *Hum. Mol. Genet.* 29:1330–1339. https://doi.org/10.1093/hmg/ddaa056

Eckhardt, J., C. Bachmann, M. Sekulic-Jablanovic, V. Enzmann, K.H. Park, J. Ma, H. Takeshima, F. Zorzato, and S. Treves. 2019. Extraocular muscle function is impaired in ryr3 $^{-/-}$ mice. *J. Gen. Physiol.* 151:929–943. https://doi.org/10.1085/jgp.201912333

Eckhardt, J., A. Ruiz, S. Koenig, M. Frieden, H. Meier, A. Schmidt, S. Treves, and F. Zorzato. 2023. Quantitative proteomic analysis of skeletal muscles from wild-type and transgenic mice carrying recessive Ryr1 mutations linked to congenital myopathies. *Elife*. 12:e83618. https://doi.org/10.7554/eLife.83618

El-Ajouz, S., E. Venturi, K. Witschas, M. Beech, A.D. Wilson, C. Lindsay, D. Eberhardt, F. O'Brien, T. Iida, M. Nishi, et al. 2017. Dampened activity of ryanodine receptor channels in mutant skeletal muscle lacking TRIC-A. *J. Physiol.* 595:4769–4784. https://doi.org/10.1113/JP273550

Elbaz, M., A. Ruiz, C. Bachmann, J. Eckhardt, P. Pelczar, E. Venturi, C. Lindsay, A.D. Wilson, A. Alhussni, T. Humberstone, et al. 2019a. Quantitative RyR1 reduction and loss of calcium sensitivity of RyR1Q1970fsX16+A4329D cause cores and loss of muscle strength. *Hum. Mol. Genet.* 28:2987–2999. https://doi.org/10.1093/hmg/ddz092

Elbaz, M., A. Ruiz, J. Eckhardt, P. Pelczar, F. Muntoni, S. Boncompagni, S. Treves, and F. Zorzato. 2019b. Quantitative reduction of RyR1 protein caused by a single-allele frameshift mutation in RYR1 ex36 impairs the strength of adult skeletal muscle fibres. *Hum. Mol. Genet.* 28:1872–1884. https://doi.org/10.1093/hmg/ddz025

Elbaz, M., A. Ruiz, S. Nicolay, C. Tupini, C. Bachmann, J. Eckhardt, S. Benucci, P. Pelczar, S. Treves, and F. Zorzato. 2020. Bi-allelic expression of the RyR1 p.A4329D mutation decreases muscle strength in slow-twitch muscles in mice. *J. Biol. Chem.* 295:10331–10339. https://doi.org/10.1074/jbc.RA120.013846

Endo, M. 1985. Calcium release from sarcoplasmic reticulum. *In* Current Topics in Membranes and Transport. F. Bronner, editor. Academic Press, Cambridge, MA. 181–230.

Fleischer, S., and M. Inui. 1989. Biochemistry and biophysics of excitation-contraction coupling. *Annu. Rev. Biophys. Biophys. Chem.* 18:333–364. https://doi.org/10.1146/annurev.bb.18.060189.002001

Franzini-Armstrong, C., and A.O. Jorgensen. 1994. Structure and development of E-C coupling units in skeletal muscle. *Annu. Rev. Physiol.* 56:509–534. https://doi.org/10.1146/annurev.ph.56.030194.002453

Jungbluth, H., S. Treves, F. Zorzato, A. Sarkozy, J. Ochala, C. Sewry, R. Phadke, M. Gautel, and F. Muntoni. 2018. Congenital myopathies: Disorders of excitation-contraction coupling and muscle contraction. *Nat. Rev. Neurol.* 14:151–167. https://doi.org/10.1038/nrneurol.2017.191

Jungbluth, H., C. Wallgren-Pettersson, and J. Laporte. 2008. Centronuclear (myotubular) myopathy. *Orphanet J. Rare Dis.* 3:26. https://doi.org/10.1186/1750-1172-3-26

Kohn, T.A., and K.H. Myburgh. 2006. Electrophoretic separation of human skeletal muscle myosin heavy chain isoforms: The importance of reducing agents. *J. Physiol. Sci.* 56:355–360. https://doi.org/10.2170/physiolsci.RP007706

Laforgia, N., M. Capozza, L. De Cosmo, A. Di Mauro, M.E. Baldassarre, F. Mercadante, A.L. Torella, V. Nigro, and N. Resta. 2018. A rare case of severe congenital RYR1-associated myopathy. *Case Rep. Genet.* 2018:6184185. https://doi.org/10.1155/2018/6184185

Lawal, T.A., J.J. Todd, and K.G. Meilleur. 2018. Ryanodine receptor 1-related myopathies: Diagnostic and therapeutic approaches. *Neurotherapeutics*. 15:885–899. https://doi.org/10.1007/s13311-018-00677-1

Lawal, T.A., J.J. Todd, J.W. Witherspoon, C.G. Bönnemann, J.J. Dowling, S.L. Hamilton, K.G. Meilleur, and R.T. Dirksen. 2020. Ryanodine receptor 1-related disorders: An historical perspective and proposal for a unified nomenclature. *Skelet. Muscle*. 10:32. https://doi.org/10.1186/s13395-020-00243-4

Lee, C.S., A. Dagnino-Acosta, V. Yarotskyy, A. Hanna, A. Lyfenko, M. Knoblauch, D.K. Georgiou, R.A. Poche, M.W. Swank, C. Long, et al. 2015. Ca(2+) permeation and/or binding to CaV1.1 fine-tunes skeletal muscle Ca(2+) signaling to sustain muscle function. *Skelet Muscle*. 5:4. https://doi.org/10.1186/s13395-014-0027-1

Lynch, P.J., J. Tong, M. Lehane, A. Mallet, L. Giblin, J.J. Heffron, P. Vaughan, G. Zafra, D.H. MacLennan, and T.V. McCarthy. 1999. A mutation in the transmembrane/luminal domain of the ryanodine receptor is associated with abnormal Ca^{2+} release channel function and severe central core disease. *Proc. Natl. Acad. Sci. USA*. 96:4164–4169. https://doi.org/10.1073/pnas.96.7.4164

Mauri, E., D. Piga, A. Govoni, R. Brusa, S. Pagliarani, M. Ripolone, R. Dilena, C. Cinnante, M. Sciacco, D. Cassandrini, et al. 2021. Early findings in neonatal cases of RYR1-related congenital myopathies. *Front. Neurol.* 12:664618. https://doi.org/10.3389/fneur.2021.664618

McCarthy, T.V., K.A. Quane, and P.J. Lynch. 2000. Ryanodine receptor mutations in malignant hyperthermia and central core disease. *Hum. Mutat.* 15:410–417. https://doi.org/10.1002/(SICI)1098-1004(200005)15:5<410::AID-HUMU2>3.0.CO;2-D

Melzer, W., A. Herrmann-Frank, and H.C. Lüttgau. 1995. The role of Ca^{2+} ions in excitation-contraction coupling of skeletal muscle fibres. *Biochim. Biophys. Acta*. 1241:59–116. https://doi.org/10.1016/0304-4157(94)00014-5

Michelucci, A., S. Boncompagni, L. Pietrangelo, T. Takano, F. Protasi, and R.T. Dirksen. 2020. Pre-assembled Ca^{2+} entry units and constitutively active Ca^{2+} entry in skeletal muscle of calsequestrin-1 knockout mice. *J. Gen. Physiol.* 152:e202012617. https://doi.org/10.1085/jgp.202012617

Mosca, B., O. Delbono, M. Laura Messi, L. Bergamelli, Z.M. Wang, M. Vukcevic, R. Lopez, S. Treves, M. Nishi, H. Takeshima, et al. 2013. Enhanced dihydropyridine receptor calcium channel activity restores muscle strength in JP45/CASQ1 double knockout mice. *Nat. Commun.* 4:1541. https://doi.org/10.1038/ncomms2496

Nicolau, S., T. Liewluck, J.A. Tracy, R.S. Laughlin, and M. Milone. 2019. Congenital myopathies in the adult neuromuscular clinic: Diagnostic challenges and pitfalls. *Neurol. Genet.* 5:e341. https://doi.org/10.1212/NXG.0000000000000341

Pérez-Schindler, J., A. Kanhere, L. Edwards, J.W. Allwood, W.B. Dunn, S. Schenk, and A. Philp. 2017. Exercise and high-fat feeding remodel transcript-metabolite interactive networks in mouse skeletal muscle. *Sci. Rep.* 7:13485. https://doi.org/10.1038/s41598-017-14081-w

Pettersen, E.F., T.D. Goddard, C.C. Huang, G.S. Couch, D.M. Greenblatt, E.C. Meng, and T.E. Ferrin. 2004. UCSF Chimera: A visualization system for exploratory research and analysis. *J. Comput. Chem.* 25:1605–1612. https://doi.org/10.1002/jcc.20084

Pietrangelo, L., A. D'Incecco, A. Ainbinder, A. Michelucci, H. Kern, R.T. Dirksen, S. Boncompagni, and F. Protasi. 2015. Age-dependent uncoupling of mitochondria from Ca^{2+} release units in skeletal muscle. *Oncotarget*. 6:35358–35371. https://doi.org/10.18632/oncotarget.6139

Pietrangelo, L., A. Michelucci, P. Ambrogini, S. Sartini, F.A. Guarnier, A. Fusella, I. Zamparo, C. Mammucari, F. Protasi, and S. Boncompagni. 2019. Muscle activity prevents the uncoupling of mitochondria from Ca^{2+} Release Units induced by ageing and disuse. *Arch. Biochem. Biophys.* 663:22–33. https://doi.org/10.1016/j.abb.2018.12.017

Ríos, E. 2010. The cell boundary theorem: A simple law of the control of cytosolic calcium concentration. *J. Physiol. Sci.* 60:81–84. https://doi.org/10.1007/s12576-009-0069-z

Ríos, E., and G. Pizarro. 1991. Voltage sensor of excitation-contraction coupling in skeletal muscle. *Physiol. Rev.* 71:849–908. https://doi.org/10.1152/physrev.1991.71.3.849

Rokach, O., M. Sekulic-Jablanovic, N. Voermans, J. Wilmshurst, K. Pillay, L. Heytens, H. Zhou, F. Muntoni, M. Gautel, Y. Nevo, et al. 2015. Epigenetic changes as a common trigger of muscle weakness in congenital myopathies. *Hum. Mol. Genet.* 24:4636–4647. https://doi.org/10.1093/hmg/ddv195

Rueden, C.T., J. Schindelin, M.C. Hiner, B.E. DeZonia, A.E. Walter, E.T. Arena, and K.W. Eliceiri. 2017. ImageJ2: ImageJ for the next generation of scientific image data. *BMC Bioinformatics*. 18:529. https://doi.org/10.1186/s12859-017-1934-z

Ruiz, A., S. Benucci, U. Duthaler, C. Bachmann, M. Franchini, F. Noreen, L. Pietrangelo, F. Protasi, S. Treves, and F. Zorzato. 2022. Improvement of

muscle strength in a mouse model for congenital myopathy treated with HDAC and DNA methyltransferase inhibitors. *Elife*. 11:e73718. https://doi.org/10.7554/eLife.73718

Saito, A., S. Seiler, A. Chu, and S. Fleischer. 1984. Preparation and morphology of sarcoplasmic reticulum terminal cisternae from rabbit skeletal muscle. *J. Cell Biol.* 99:875–885. https://doi.org/10.1083/jcb.99.3.875

Sarkozy, A., M. Sa, D. Ridout, M.A. Fernandez-Garcia, M.G. Distefano, M. Main, J. Sheehan, A.Y. Manzur, P. Munot, S. Robb, et al. 2023. Long-term natural history of pediatric dominant and recessive RYR1-related myopathy. *Neurology*. 101:e1495–e1508. https://doi.org/10.1212/WNL.0000000000207723

Schiaffino, S., A.C. Rossi, V. Smerdu, L.A. Leinwand, and C. Reggiani. 2015. Developmental myosins: Expression patterns and functional significance. *Skelet. Muscle*. 5:22. https://doi.org/10.1186/s13395-015-0046-6

Shapovalov, M.V., and R.L. Dunbrack Jr. 2011. A smoothed backbone-dependent rotamer library for proteins derived from adaptive kernel density estimates and regressions. *Structure*. 19:844–858. https://doi.org/10.1016/j.str.2011.03.019

Shishmarev, D. 2020. Excitation-contraction coupling in skeletal muscle: Recent progress and unanswered questions. *Biophys. Rev.* 12:143–153. https://doi.org/10.1007/s12551-020-00610-x

Sitsapesan, R., R.A. Montgomery, K.T. MacLeod, and A.J. Williams. 1991. Sheep cardiac sarcoplasmic reticulum calcium-release channels: Modification of conductance and gating by temperature. *J. Physiol.* 434:469–488. https://doi.org/10.1113/jphysiol.1991.sp018481

Stringer, C., T. Wang, M. Michaelos, and M. Pachitariu. 2021. Cellpose: A generalist algorithm for cellular segmentation. *Nat. Methods*. 18:100–106. https://doi.org/10.1038/s41592-020-01018-x

Talmadge, R.J., and R.R. Roy. 1993. Electrophoretic separation of rat skeletal muscle myosin heavy-chain isoforms. *J. Appl. Physiol.* 75:2337–2340. https://doi.org/10.1152/jappl.1993.75.5.2337

Tjondrokoesoemo, A., K.H. Park, C. Ferrante, S. Komazaki, S. Lesniak, M. Brotto, J.K. Ko, J. Zhou, N. Weisleder, and J. Ma. 2011. Disrupted membrane structure and intracellular Ca^{2+} signaling in adult skeletal muscle with acute knockdown of Bin1. *PLoS One*. 6:e25740. https://doi.org/10.1371/journal.pone.0025740

Treves, S., H. Jungbluth, F. Muntoni, and F. Zorzato. 2008. Congenital muscle disorders with cores: The ryanodine receptor calcium channel paradigm. *Curr. Opin. Pharmacol.* 8:319–326. https://doi.org/10.1016/j.coph.2008.01.005

Tubridy, N., B. Fontaine, and B. Eymard. 2001. Congenital myopathies and congenital muscular dystrophies. *Curr. Opin. Neurol.* 14:575–582. https://doi.org/10.1097/00019052-200110000-00005

Venturi, E., E. Galfré, F. O'Brien, S.J. Pitt, S. Bellamy, R.B. Sessions, and R. Sitsapesan. 2014. FKBP12.6 activates RyR1: Investigating the amino acid residues critical for channel modulation. *Biophys. J.* 106:824–833. https://doi.org/10.1016/j.bpj.2013.12.041

Waisman, A., A.M. Norris, M. Elías Costa, and D. Kopinke. 2021. Automatic and unbiased segmentation and quantification of myofibers in skeletal muscle. *Sci. Rep.* 11:11793. https://doi.org/10.1038/s41598-021-91191-6

Wei-LaPierre, L., L. Groom, and R.T. Dirksen. 2022. Acute exposure to extracellular BTP2 does not inhibit Ca^{2+} release during EC coupling in intact skeletal muscle fibers. *J. Gen. Physiol.* 154:e202112976. https://doi.org/10.1085/jgp.202112976

Wieczorek, D.F., M. Periasamy, G.S. Butler-Browne, R.G. Whalen, and B. Nadal-Ginard. 1985. Co-Expression of multiple myosin heavy chain genes, in addition to a tissue-specific one, in extraocular musculature. *J. Cell Biol.* 101:618–629. https://doi.org/10.1083/jcb.101.2.618

wwPDB consortium. 2019. Protein Data Bank: The single global archive for 3D macromolecular structure data. *Nucleic Acids Res.* 47:D520–D528. https://doi.org/10.1093/nar/gky949

Zorzato, F., H. Jungbluth, H. Zhou, F. Muntoni, and S. Treves. 2007. Functional effects of mutations identified in patients with multiminicore disease. *IUBMB Life*. 59:14–20. https://doi.org/10.1080/15216540601187803

Supplemental material

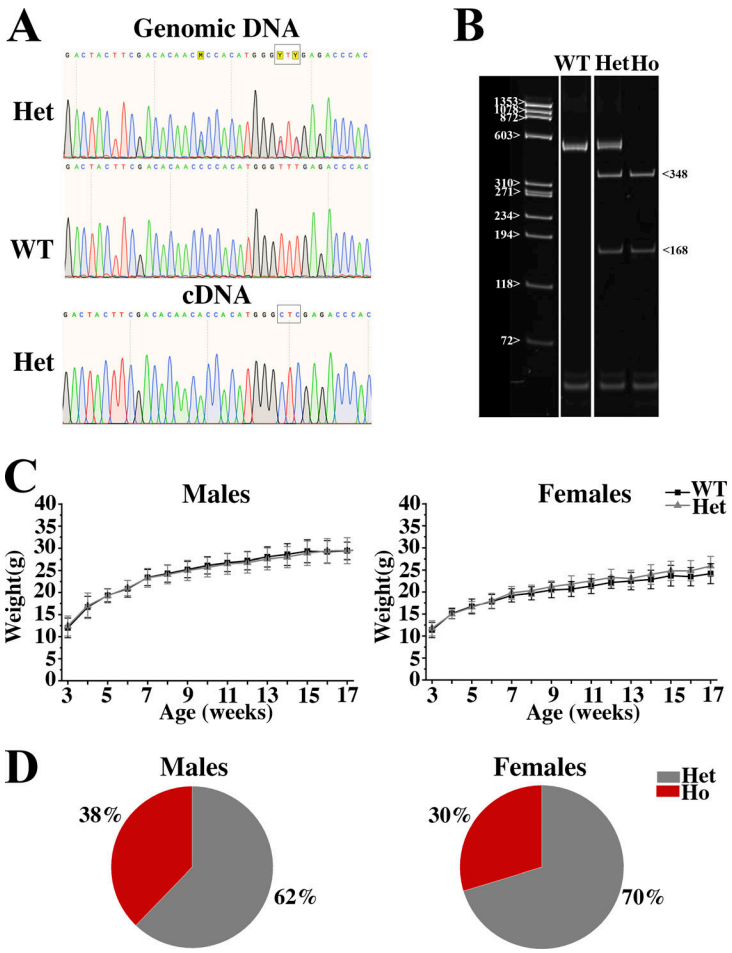

Figure S1. **Representative data of Het and Ho transgenic p.F4976L *RyR1* mutant mice. (A)** Confirmation of the presence of the p.F4976L *Ryr1* mutation in the genomic DNA of heterozygous mice (upper panel) and in the cDNA (lower panel) of heterozygous mice. **(B)** Digestion of PCR amplified cDNA with *XhoI* for genotyping. In the genomic DNA from WT mice, the 516 bp PCR fragment is not cut by the restriction enzyme since it lacks the engineered XhoI site. In the Het mice, the mutant allele yields stoichiometric fragments of 516, 348, and 168 bp after digestion with XhoI. In the Ho mice, both alleles are digested resulting in 348 and 168 bp fragments. **(C)** Growth curves of Het mice compared with WT mice from male (left) and female (right) mice. **(D)** Decreased frequency of male and female Ho pups in Ho × Het breeding pairs ($P < 0.05$ using the $\chi 2$ test, with a two-tailed P value). The expected frequency would be 50% for both genotypes. Total number of males mice = 90, total number of females mice = 64.

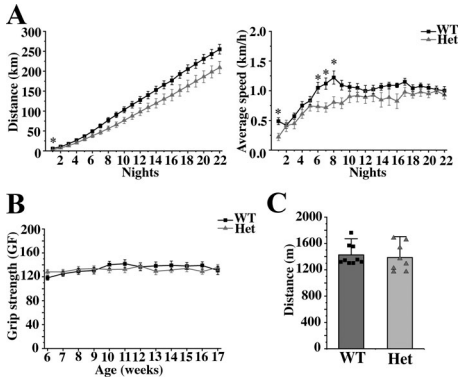

Figure S2. **In vivo measurements of muscle function in Het p.F4976L mice. (A)** Comparison of the total running distance (left) and average speed (right) of Het mice (grey symbols; *n* = 10) and WT (black symbols; *n* = 13) littermates. Each point represents the mean ± SEM ($P < 0.05$ using ANOVA followed by the Bonferroni post-hoc test). **(B)** Forelimb muscle grip strength of Het (*n* = 17) mice and WT (*n* = 15) littermates. No difference in strength was observed at any timepoint. Each point represents the mean (±SEM) of five measurements. **(C)** Treadmill running distance (in m) to exhaustion in Het and WT littermates. No significant difference between the two genotypes was observed. Mean distance to exhaustion run by Het and WT was 1,387 ± 211 and 1,426 ± 164 m, respectively. Each symbol represents the value from a single mouse; bars represent mean ± SD.

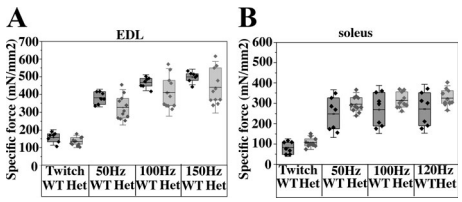

Figure S3. **Mechanical properties of EDL and soleus muscles from WT and Het p.F4976L mice. (A and B)** Specific force values of EDL (A) and soleus (B) muscles from Het mice compared to WT littermates. No significant difference between the two genotypes was observed. In EDL, the mean (±SD) specific force developed after twitch stimulation was 136 ± 23 and 158 ± 29 for Het and WT, respectively, while for the 150 Hz tetani, it was 442 ± 97 and 499 ± 30. For soleus twitch in Het, the mean ± SD was 108 ± 23 and in WT 83 ± 29, while for the Het 120 HZ tetanic stimulation it was 326 ± 41, and for WT 274 ± 78. Each symbol corresponds to a mouse, whiskers show SD. Het *n* = 11, WT = 7.

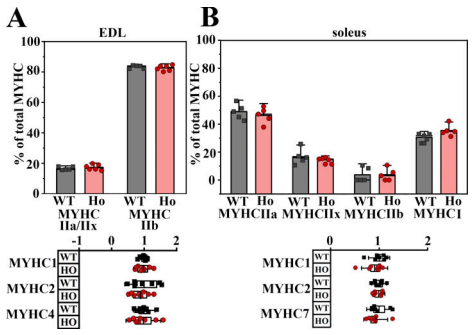

Figure S4. **MyHC expression in muscles from WT and Ho. (A and B)** Top: MyHC protein content by quantification of Coomassie Blue stained acrylamide gels in EDL and soleus muscles. Bottom: qPCR of MyHC isoform expression.

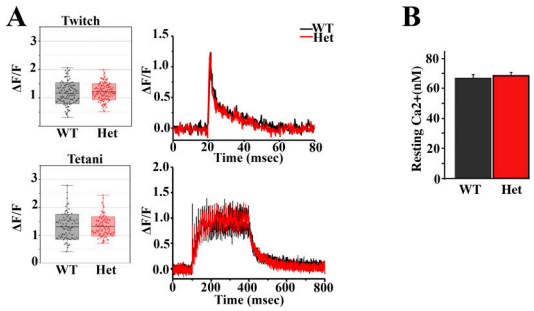

Figure S5. **Calcium homeostasis is not affected in FDB fibers from p.F4976L Het mice. (A)** Left panels: Box plots of peak calcium released after twitch and tetanic stimulation (top and lower panels, respectively) (*n* fibers for twitch WT = 122, *n* fibers for Het = 143, *n* fibers for tetani WT = 88, *n* fibers for tetani Het = 98, 6 mice per group). Right panels: Representative traces of electrically evoked calcium release after twitch and tetanic stimulation of FDB from WT (black races) and Het (red traces). **(B)** Resting calcium in FDB fibers from WT and Het mice (*n* fibers WT = 91, *n* fibers Het = 111). Bars show mean ± SEM.

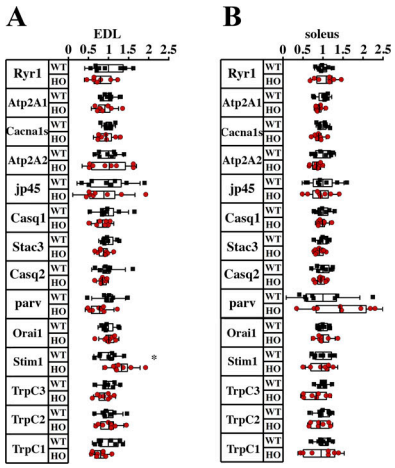

Figure S6. **Analysis of transcript expression in muscles from WT and p.F4976L Ho mice. (A and B)** qPCR analysis of main transcripts encoding proteins involved in ECC and calcium homeostasis in EDL and soleus muscles from WT and Ho mice. Values of transcripts were normalized to the housekeeping muscle gene *Actn2*. Each symbol represents values from a single mouse. *P < 0.05 Mann–Whitney test.

Provided online are five tables. Table S1 lists the sequence of primers and target genes. Table S2 provides a list of antibodies and suppliers. Table S3 lists twitch and tetanic parameters for both EDL and soleus muscles of homozygous and WT mice. Table S4 shows force kinetic values of EDL and soleus muscles of homozygous and WT mice. Table S5 provides an analysis of the kinetic parameters of electrically evoked Ca^{2+} transients in FDB fibers from Ho, Het, and WT mice.